

Visualizing a protonated RNA state that modulates microRNA-21 maturation

Jared T. Baisden ¹, Joshua A. Boyer ¹, Bo Zhao ^{1,2}, Scott M. Hammond and Qi Zhang ¹

MicroRNAs are evolutionarily conserved small, noncoding RNAs that regulate diverse biological processes. Due to their essential regulatory roles, microRNA biogenesis is tightly regulated, where protein factors are often found to interact with specific primary and precursor microRNAs for regulation. Here, using NMR relaxation dispersion spectroscopy and mutagenesis, we reveal that the precursor of oncogenic microRNA-21 exists as a pH-dependent ensemble that spontaneously reshuffles the secondary structure of the entire apical stem-loop region, including the Dicer cleavage site. We show that the alternative excited conformation transiently sequesters the bulged adenine into a noncanonical protonated A+-G mismatch, conferring a substantial enhancement in Dicer processing over its ground conformational state. These results indicate that microRNA maturation efficiency may be encoded in the intrinsic dynamic ensemble of primary and precursor microRNAs, providing a potential means of regulating microRNA biogenesis in response to environmental and cellular stimuli.

icroRNAs (miRNAs) are highly conserved, small noncoding RNAs that regulate more than 60% of protein coding genes at the posttranscriptional level¹⁻⁵. Due to their essential regulatory roles, miRNA biogenesis is tightly regulated to ensure proper gene expression³⁻⁵, and abnormal miRNA regulation has often been associated with cancer, neurological disorders, cardiovascular diseases and other diseases^{6,7}. Remarkably, despite sharing the same set of enzymes in the canonical biogenesis pathway3, individual miRNAs exhibit cell type- and cell state-specific expressions, where even those clustered on the same primary transcript can be differentially processed in a tissue-specific manner³⁻⁵. Over the past decade, it has been shown that specific sequences and structures of primary and precursor miRNAs can be recognized by processing machineries and protein factors for regulation⁸⁻¹⁹. For example, pri-miRNAs that possess a UGU motif in the apical loops are preferentially processed by the Microprocessor^{11,12}, pre-miRNAs encoding a two-nucleotide distance between the cleavage sites and the apical bulge/loop structures are more accurately processed by Dicer¹³ and miRNAs that feature stable basal stems in pri-miRNAs and flexible apical loops in pri-/pre-miRNAs are more efficiently processed by biogenesis machineries¹⁴. In addition, altering secondary structures and even primary sequences of pri-/pre-miRNAs via protein binding¹⁵, enzymatic-driven nucleotide modification^{16,17}, disease-linked mutation¹⁸ and other molecular signals¹⁹ can further influence the outcome of miRNA biogenesis³. During these regulatory processes, it is often perceived that protein factors act on the largely passive primary and precursor miRNAs to direct their maturation outcome. However, despite many noncoding RNAs having been shown to actively explore their conformational dynamics for function²⁰, it remains elusive as to whether pri-/pre-miRNAs can play a role in modulating miRNA biogenesis in the absence of protein factors. This is largely due to our limited high-resolution structural and dynamic knowledge of most pri-/pre-miRNAs, where key regulatory elements of pri-/pre-miRNAs, such as the apical stem-loop region, also known as the pre-element region, are

often too flexible to be studied by conventional structural biology approaches.

Here, we set out to characterize the structural dynamics of microRNA-21 precursor (pre-miR-21) and examine how the intrinsic RNA conformational plasticity may contribute to miRNA maturation. MicroRNA-21, one of the first identified human miRNAs21, functions as an oncogene involved in tumorigenesis, progression, metastasis and cell survival²², where its biogenesis is regulated at both the transcriptional and posttranscriptional levels²³. Previous studies have shown that the pre-element region of pri-/pre-miR-21 serves as an important element for regulating miR-21 biogenesis. Mutations that stabilize the pre-element inhibit Microprocessor processing of pri-miR-21 (ref. ²⁴), whereas binding of the KH-type splicing regulatory protein at this location promotes enzymatic processing of pri-/ pre-miR-21s²⁵. By carrying out NMR relaxation dispersion (RD) and chemical exchange saturation transfer (CEST) measurements, we discovered that the pre-element region of pri-/pre-miR-21 exists as a pH-dependent two-state ensemble, which dynamically accesses a low-populated (~1-15%) transient, yet kinetically stable (lifetime ~0.8 ms) state, referred to as an excited state (ES), across physiologically relevant ranges of pH (pH ~6.5–8.0). N1 protonation sequesters the adenine at the Dicer cleavage site from a bulged residue in the ground-state (GS) conformation into a noncanonical $A^+(anti)$ -G(syn)base pair in the ES, which closely resembles the optimal substrate structure for Dicer processing, where both cleavage sites reside within a double-stranded helical conformation and are positioned two nucleotides away from a flexible apical loop¹³. We further demonstrated that these distinct structures are processed differently by Dicer, where the ES-mimicking substrate is processed to mature miR-21 with a 4- and 28-fold enhancement in efficiency over its GS counterpart at pH7.77 and 6.51, respectively. With the emerging view of the RNA ES as a 'hidden' layer for regulation²⁰, our results suggest that miRNA-processing intermediates may employ ES-encoded dynamic ensembles as a potential means to regulate microRNA biogenesis in response to environmental and cellular stimuli.

¹Department of Biochemistry and Biophysics, University of North Carolina at Chapel Hill, Chapel Hill, NC, USA. ²Department of Chemistry, University of North Carolina at Chapel Hill, Chapel Hill, NC, USA. ³Department of Cell Biology and Physiology, University of North Carolina at Chapel Hill, NC, USA. ^{Se-mail: zhangqi@unc.edu}

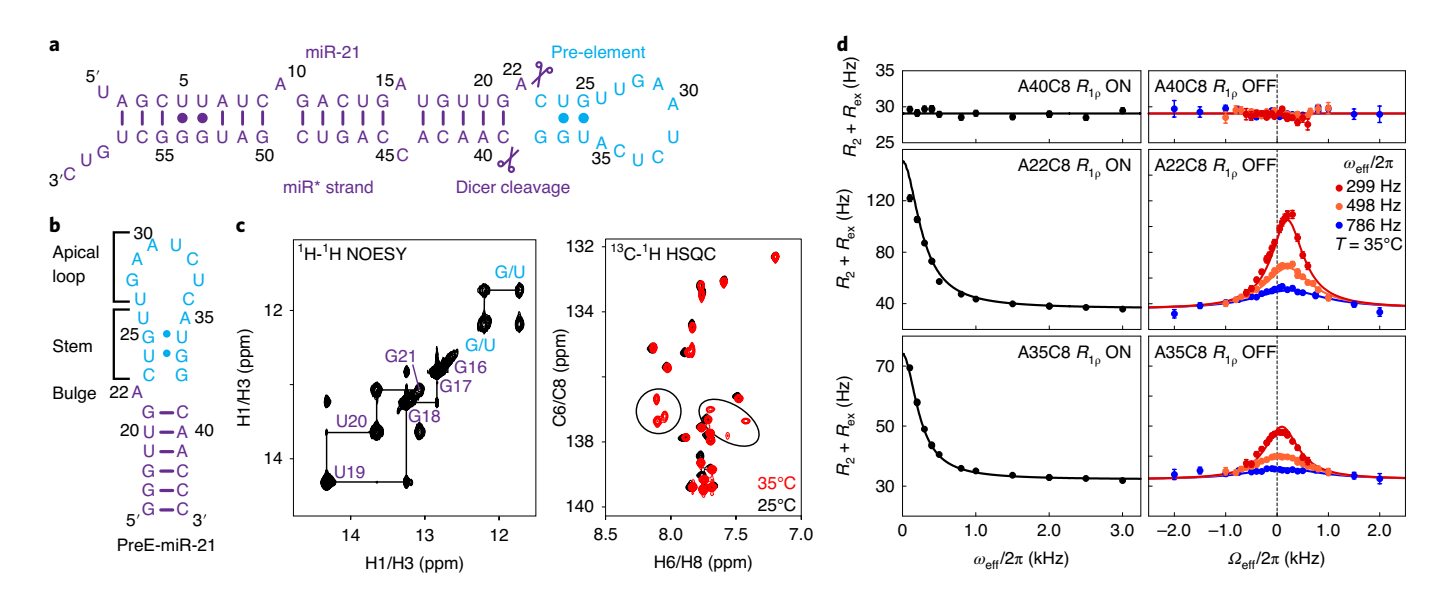


Fig. 1 | NMR characterization of preE-miR-21. a, Secondary structure of pre-miR-21 with Dicer cleavage sites highlighted as scissors. **b**, Secondary structure of preE-miR-21 construct derived from NMR data, where Watson-Crick base pairs, G • U wobbles and potential Watson-Crick base pairs are highlighted with lines, filled circles and open circles, respectively. **c**, NMR ¹H-¹H NOESY spectrum of the imino proton region of preE-miR-21 at 10 °C and ¹³C-¹H HSQC spectra of the base carbon (C6 and C8) region of preE-miR-21 at 25 °C and 35 °C at pH 6.45. **d**, Representative ¹³C on-resonance and off-resonance RD profiles at 35 °C and pH 6.45 showing dependence of $R_2 + R_{ex}$ on spin-lock power ($ω_{eff}/2π$) and offset (Ω/2π), respectively, where Ω is the difference between the spin-lock carrier frequency and the observed resonance frequency. RD profiles of A40 are fit to a single-state model and RD profiles of A22 and A35 are fit to a global two-state model using the Bloch-McConnell equation. Shown are the best-fit values and experimental uncertainties (s.d.) estimated from monoexponential fitting of n = 3 independently measured peak intensities.

Results

Pre-miR-21 samples distinct conformational states. The miR-21 precursor consists of the pre-element region and miR-21/miR-21* helix, and is predicted to fold into a hairpin structure with four double-stranded helices, three bulges and one apical loop (Fig. 1a). To focus on the pre-element region, we designed a shorter RNA construct, preE-miR-21, which contains the entire pre-element and the adjacent helix from the miR-21/miR-21* stem (Fig. 1b). NMR ¹H-¹H NOESY experiments on the imino region provide excellent characterization of the RNA secondary structure, as one imino resonance is expected for a canonical Watson-Crick base pair and two imino resonances are expected for a GoU wobble pair. Except for the formation of Watson-Crick base pairs at the lower stem, the pre-element of miR-21 does not adopt a stable conformation, as only weak imino resonances of G•U wobble pairs can be observed in the NMR ¹H-¹H NOESY spectrum (Fig. 1c). This observation is consistent with previous NMR studies on the miR-21 precursor^{26,27}, where mutations of the pre-element were made to quench the structural flexibility into a single conformational state²⁶. When we carried out an NMR 13C-1H HSQC experiment that probes nonsolvent-exchangeable signals, surprisingly, only 20 out of a total of 29 expected NMR resonances from preE-miR-21 were observed at room temperature and pH 6.45 (Fig. 1c). This spectroscopic behavior resembles the typical NMR phenomenon of exchange broadening, where interconversion between two or more states can lead to the disappearance of NMR signals. Indeed, by raising the temperature from 25 °C to a more physiologically relevant 35 °C, most of the missing resonances reappeared in the NMR ¹³C-¹H HSQC spectrum (Fig. 1c), confirming the presence of conformational exchange.

Recent developments of NMR $R_{1\rho}$ RD spectroscopy have opened up new avenues to quantify microsecond-to-millisecond conformational changes and made it possible to study RNA ESs that are too low in population and too short-lived to be detected by conventional techniques^{28–32}. Here, we carried out both on-resonance and off-resonance low spin-lock field $R_{1\rho}$ RD experiments to quantify

the exchange process in preE-miR-21 at 35 °C, the condition that provided the most complete NMR resonances for characterizing dynamics and which was used for all subsequent RD experiments. For residues from the miR-21/miR-21* stem region, we observed flat RD profiles for base (C2, C5, C6 and C8) and sugar (C1') carbons (Fig. 1d and Extended Data Fig. 1), which are consistent with one stable helical conformation of this region. In contrast, residues within the pre-element region, ranging from the bulge residue A22 to the stem residue A35 (Fig. 1d and Extended Data Fig. 2), display power and offset-dependent RD profiles. Indeed, these RD profiles can be global-fitted to a single two-state (GS↔ES) exchange process. These results reveal that the pre-element region is not only conformationally flexible, but also dynamically interconverts between at least two structurally and kinetically distinct states at 35 °C and pH 6.45, where the ES has a low population (p_{ES}) of 15.2 \pm 0.3% and a short lifetime ($\tau_{ES} = 1/k_{EG}$) of $816 \pm 15 \,\mu s$ (Fig. 1d).

ES is transiently protonated at the Dicer cleavage site. To gain structural insights into the ES, we examined ES carbon chemical shifts $(\varpi_{FS} = \varpi_{GS} + \Delta \varpi)$, where $\Delta \varpi$ is the chemical-shift difference between the ES (ϖ_{ES}) and GS (ϖ_{GS}) extracted from the two-state analysis of an R_{10} RD profile (Extended Data Fig. 3). Among all the extracted ES chemical shifts, the base carbon C8 of bulge A22, which resides at the Dicer cleavage site, displays the largest deviation ($\Delta \varpi$) with an ~1.49 ppm downfield shift from its GS position (Fig. 1d and Extended Data Fig. 3). Notably, we were not able to obtain the RD profile for base carbon C2 of A22, as the C2H2 resonance remains severely broadened beyond detection in the NMR ¹³C-¹H HSQC spectrum (Fig. 2a), suggesting even larger perturbations in carbon C2 and/or proton H2 chemical shifts between ES and GS. The dramatically different behavior of C8H8 and C2H2 resonances from the same base is reminiscent of recent NMR studies on transiently N1-protonated adenines^{33,34}.

To examine whether the exchange process could be due to possible protonation events, we increased the pH of the sample from

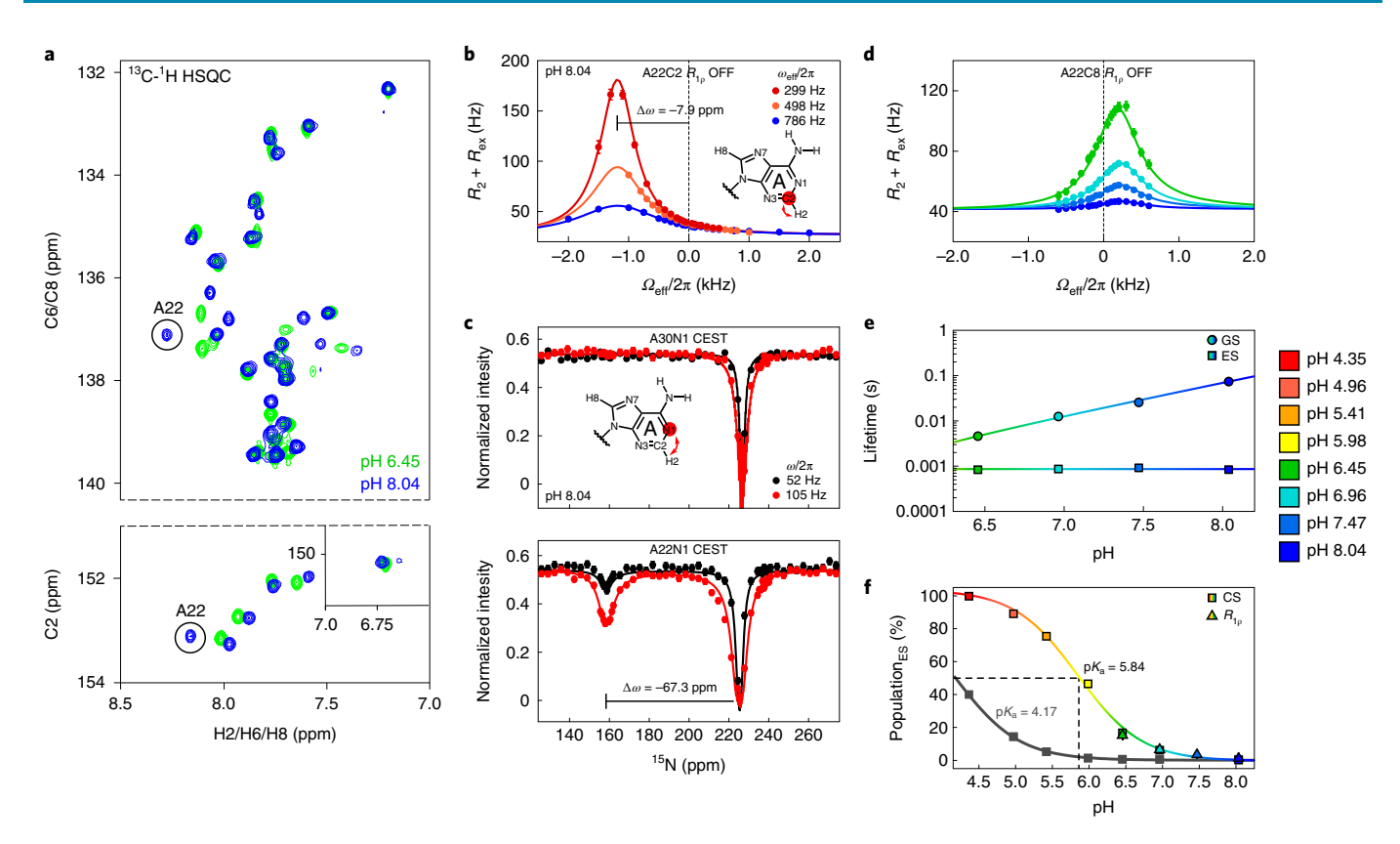


Fig. 2 | PreE-miR-21 populates a protonated excited state with a neutral-shifted pK_a, a, NMR 13 C- 1 H HSQC spectra of the base carbon (C2, C6 and C8) region of preE-miR-21 at pH 6.45 and pH 8.04 at 35 $^{\circ}$ C. **b**, 13 C off-resonance RD profiles of A22-C2 at pH 8.04 and 35 $^{\circ}$ C. **c**, 15 N CEST profiles of A30-N1 and A22-N1 at pH 8.04 and 35 $^{\circ}$ C, which are fit to a single-state and a two-state model, respectively, using the Bloch-McConnell equation. **d**, The pH-dependent 13 C off-resonance RD profiles of A35-C8 at spin-lock power of $ω_{eft}/2π = 299$ Hz. **e**, The pH-dependent apparent lifetimes of GS and ES from RD analysis. **f**, The pH-dependent population of the excited state based on R_{1p} RD data and A22-C8 chemical shift (CS) for extracting an apparent pK_a of A22. Representative pK_a derived from unpaired A29, A30 and A35 are shown in black. Shown are best-fit values and experimental uncertainties (s.d.) estimated from monoexponential fitting of n = 3 independently measured peak intensities.

6.45 to 8.04, aiming to shift the equilibrium towards nonprotonated states. Indeed, the NMR 13C-1H HSQC spectrum recorded at pH 8.04 exhibits much higher quality, where exchange broadening of most resonances is substantially reduced, such that the A22-C2H2 resonance can be readily observed (Fig. 2a). NMR RD measurements provide further quantitative support for a protonated ES of preE-miR-21 (Fig. 2b and Extended Data Fig. 4). Global fit of RD profiles showed that the GS↔ES equilibrium is substantially shifted towards the GS at pH 8.04, where the ES population (p_{ES}) is reduced from $15.2 \pm 0.3\%$ at pH 6.45 to a mere $1.1 \pm 0.1\%$ at pH 8.04. In addition, a two-state analysis of the RD profile of base carbon A22-C2 further revealed a remarkable 7.9-ppm difference between its GS and ES chemical shifts, resulting in an ES chemical shift of 144.5 ppm (Fig. 2b and Extended Data Fig. 5). This upfield shifted C2 chemical shift is consistent with C2 chemical shifts reported for stably N1-protonated adenines, strongly suggesting that A22 is protonated at the N1 site in the ES.

Recently, we have developed nucleic acid-specific ¹⁵N CEST NMR spectroscopy using nonproton-bonded nitrogens³⁵, enabling direct evaluation of the ES protonation status of adenines, which has remained elusive to date. By measuring ¹⁵N CEST profiles at pH 8.04, we were able to unambiguously identify that A22 is transiently protonated at N1 (Fig. 2c). Unlike N1 of A30, which is not protonated and displays an apparent single-dip CEST profile, the nitrogen CEST profile of A22-N1 exhibits two distinct intensity dips that correspond to two alternative conformations. A two-state analysis of the CEST profile validates that A22-N1 probes the same

two-state exchange process, where the extracted ES population ($p_{\text{ES-CEST}} \approx 1.1 \pm 0.1\%$) and lifetime ($\tau_{\text{ES-CEST}} \approx 645 \pm 114\,\mu\text{s}$) from ^{15}N CEST are very similar to those obtained from ^{13}C R_{1p} RD at pH 8.04 ($p_{\text{ES-R1p}} \approx 1.1 \pm 0.1\%$, $\tau_{\text{ES-R1p}} \approx 823 \pm 109\,\mu\text{s}$). The ES chemical shift of A22-N1 directly supports a protonated N1 with an unprecedented upfield shift of 67.3 \pm 0.2 ppm to 157.7 ppm, residing well among resonances of proton-bonded imino nitrogens in RNA (~134–152 ppm in G and ~154–165 ppm in U).

To obtain more insights into the A22 (GS)↔A22+ (ES) transition, we further carried out carbon R_{10} RD and nitrogen CEST measurements on base (C2, C8, N1) and sugar (C1') moieties of A22 at pH 6.96 and 7.47 (Fig. 2d and Extended Data Fig. 5). Consistent with being a protonation-dependent process, the population of A22+ gradually increases from ~1% at pH 8.04 to ~15% at pH 6.45. Surprisingly, the lifetime of the ES A22+ remains largely unperturbed between pH 6.45 and pH 8.04, where the average lifetime is $\tau_{ES} \approx 847 \pm 49 \,\mu s$ (Fig. 2e). In contrast, the apparent lifetime of the GS, which is derived from the extracted rate of exchange $(\tau_{\rm GS} = 1/k_{\rm GE})$, reduces substantially from $\tau_{\rm GS} \approx 74\,\rm ms$ at pH 8.04 to $\tau_{GS} \approx 5 \,\text{ms}$ at pH 6.45 (Fig. 2e). The high population of A22⁺ at pH 6.45, which otherwise would be close to zero on the basis of the intrinsic p K_a (~3.5) of the free adenine N1 site³⁶, further suggests that A22 has a distinct protonation propensity when compared with other unstructured adenines. Consistent with this observation, pH-dependent chemical-shift analyses showed a p K_a value of 5.84 ± 0.08 for A22, which is substantially shifted towards neutral pH from adenines in the apical loop that have an average pK_a value

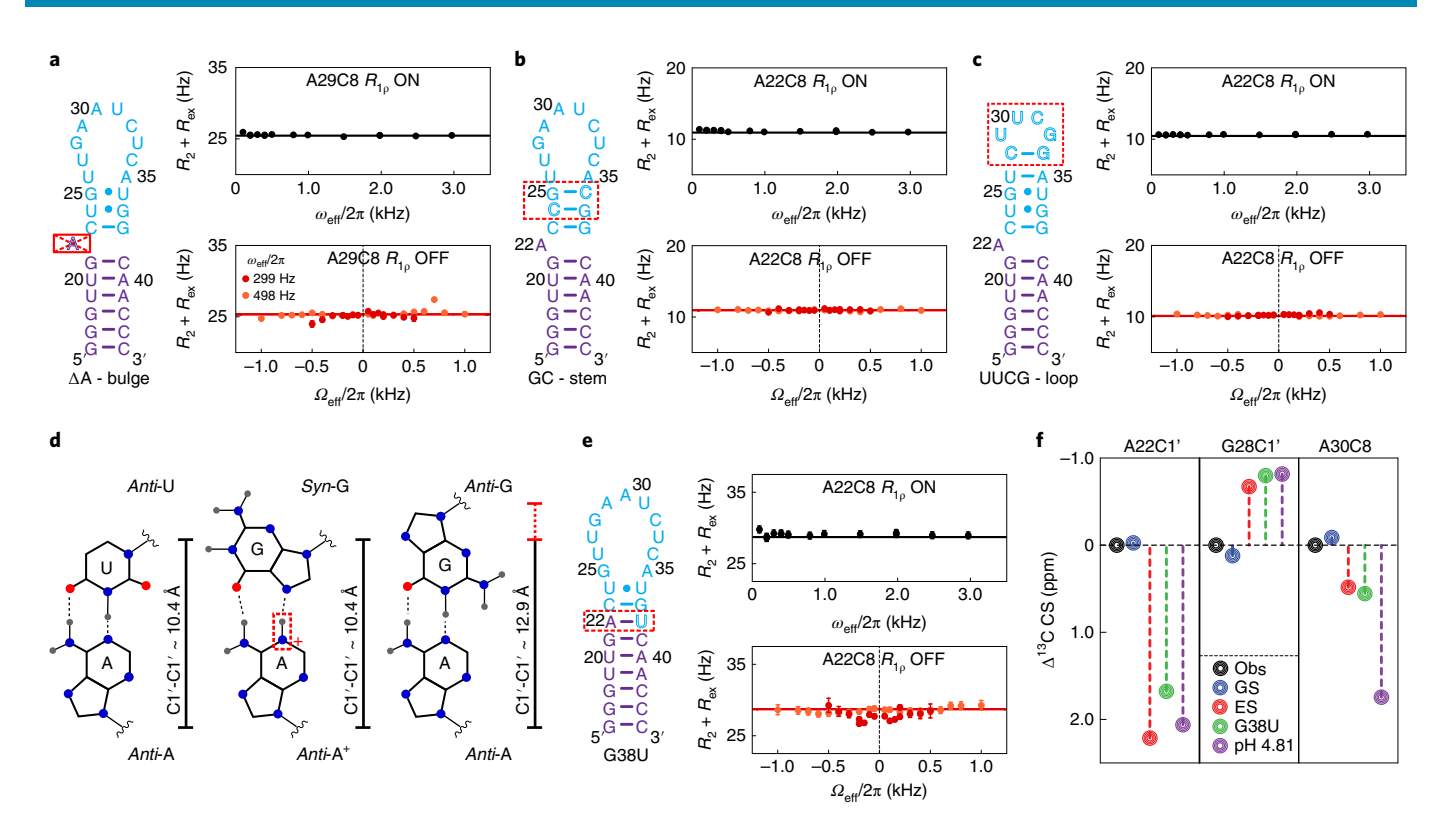


Fig. 3 | Excited-state structure of preE-miR-21. a-c, Secondary structures and representative ¹³C on-resonance and off-resonance RD profiles of bulge (a), stem (b) and loop (c) mutants. d, Sugar-sugar (C1'-C1') distances of A-U Watson-Crick base pair, A-G mismatch and A+-G mismatch. e, Secondary structure and representative ¹³C on-resonance and off-resonance RD profiles of the ES-mimic mutant. f, Comparison of carbon chemical shifts for the GS, ES (the mutant mimics) and the wild-type construct at pH 4.81. Shown are the best-fit values and experimental uncertainties (s.d.) estimated from monoexponential fitting of *n*=3 independently measured peak intensities.

of 4.17 ± 0.06 (Fig. 2f and Extended Data Fig. 6). Taken together, these results unambiguously revealed that preE-miR-21 undergoes a pH-dependent conformational transition, where A22 at the Dicer cleavage site is specifically protonated in the ES.

The protonation couples global structural reshuffling. How does the ES stabilize a site-specific protonation? To address this, we first evaluated each structural motif of the pre-element regionthe bulge, the stem and the apical loop (Fig. 3a-c and Extended Data Fig. 7). Bulge A22 is the site of protonation. Without A22, we could not detect any conformational exchange within the rest of the pre-element region, as evidenced by flat RD profiles for the A22-deletion mutant (Fig. 3a). Not only is a protonated A22 the result of the structural transition, but also this protonation may likely be the chemical basis that triggers the larger transition across the entire pre-element region. In addition to the indispensable bulge A22, we found that both a weak stem and a flexible apical loop are needed to achieve the structural transition. Stabilizing the two G•U wobble pairs with G-C Watson-Crick pairs completely quenches the exchange (Fig. 3b); replacing the apical loop with a highly structured UUCG tetraloop also eliminates the transition (Fig. 3c). These results suggest that the pre-element region serves as a unified structural entity to enable a concerted transition towards stabilizing the protonated ES. The rate of exchange $(k_{\rm ex} = k_{\rm GE} + k_{\rm EG} \approx 1,445 \, \rm s^{-1})$ is an order of magnitude slower than rates observed from local structural changes involving transient adenine protonation³⁷, but similar to the secondary structure-based long-range communication observed in HIV-1 TAR RNA³⁸, further supporting a global secondary structural reshuffling of the pre-element region.

To delineate the ES secondary structure, we employed a mutate-and-chemical-shift-fingerprinting strategy³⁷. Here, we first

used MC-fold³⁹ to predict possible alternative low-energy secondary structures of preE-miR-21. Strikingly, most of the predicted structures share a common feature of an A22-G38 base pair, whereas the remaining pre-element adopts various secondary structures that are distinct from the ground-state conformation (Extended Data Fig. 8). Being protonated at N1, A22 could potentially be base paired with G38 in the ES, albeit in the A⁺(anti)-G(syn) form rather than the conventional A(anti)-G(anti) pair, where the syn conformation of G38 is indicated with the downfield chemical shift of base carbon C8 ($\Delta \varpi_{ES}$ = 2.6 ppm) at pH 8.04 (Extended Data Fig. 4). An interesting structural feature of the A⁺(anti)-G(syn) pair is that it largely retains an overall A-form-like geometry, with an intersugar distance of 10.4 Å (ref. ⁴⁰), whereas the A(anti)-G(anti) pair substantially widens this distance to 12.9 Å (ref. ⁴¹) and subsequently distorts the helical geometry of neighboring base pairs (Fig. 3d).

To test this proposed ES structural feature, we mutated G38 to a uridine, which not only sequesters A22 into a base pair, but also maintains an A-form geometry at the site of mutation. The G38U mutant converges into a single state as evidenced by flat RD profiles (Fig. 3e and Extended Data Fig. 9), and largely represents the ES of preE-miR-21 on the basis of chemical shifts. Good agreement was observed between chemical-shift differences between the mutant and wild type ($\Delta \varpi_{\rm G38U}$) and those extracted from NMR RD profiles $(\Delta \varpi_{RD})$ for 15 out of 19 base and sugar carbon resonances from the pre-element residues with detectable RD profiles, including A22(C1'), C23(C1'), G28(C1'), A29(C2/C8), A30(C8), U31(C1'), C32(C1'), U33(C6), C34(C6), A35(C1'/C2/C8), U36(C6) and C39(C5) (Fig. 3f and Extended Data Figs. 3 and 4). The agreement of sugar carbon C1's of A22 and C23 further supports the ES adopting an A-form-like backbone geometry at the site of protonation. The deviations between $\Delta\varpi_{\text{G38U}}$ and $\Delta\varpi_{\text{RD}}$ for base carbons

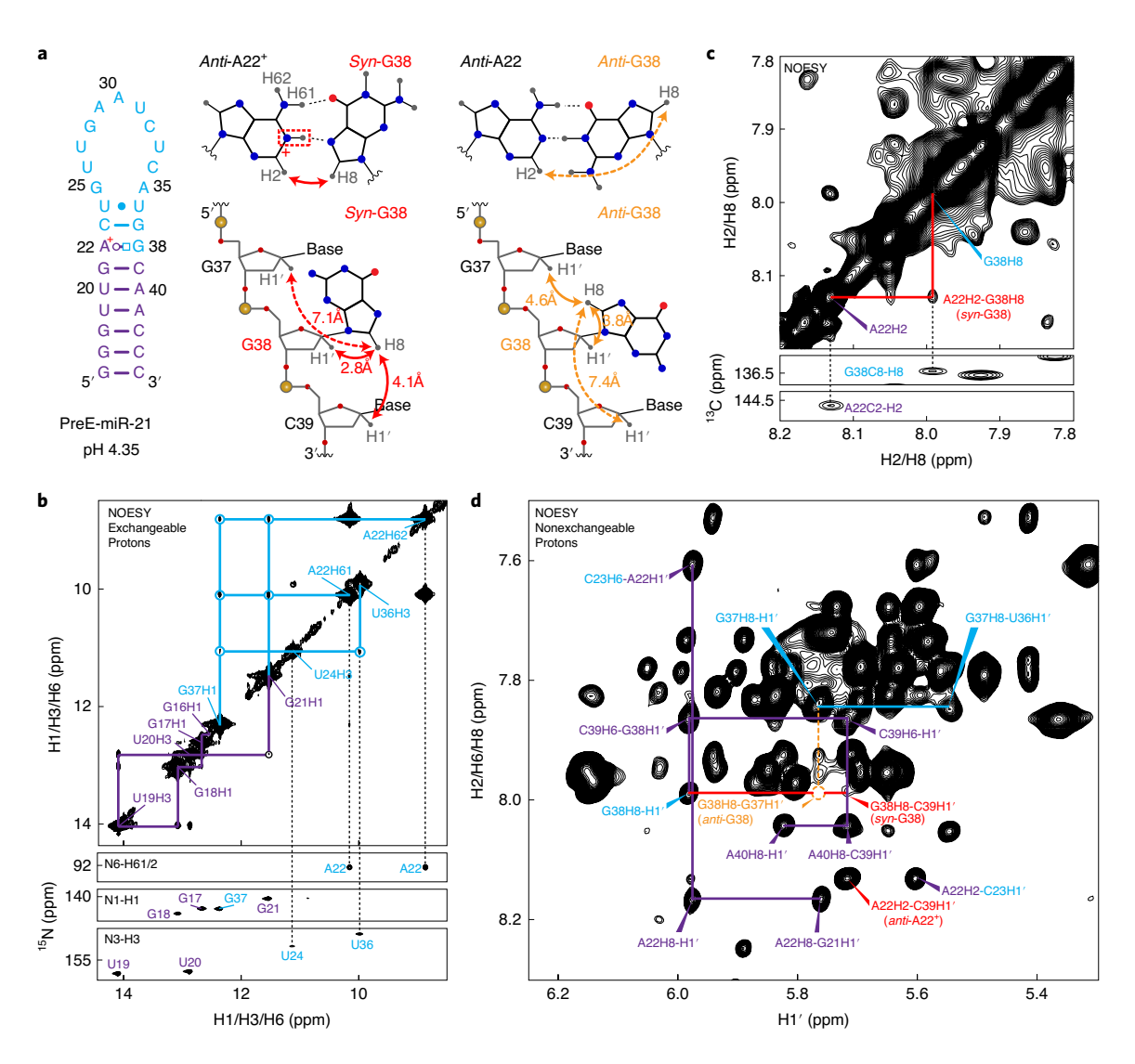


Fig. 4 | NMR characterization of protonated preE-miR-21 at low pH. a, Secondary structure of preE-miR-21 at pH 4.35, where A22 is protonated at the N1 site. Schematic diagrams that depict observable (solid arrows) and unobservable (dashed arrows) 'H-'H NOE cross-peaks in the A22-G38 pair with G38 adopting either *syn* or *anti* conformation. Interproton distances in A+(*anti*)-G38(*syn*) and A(*anti*)-G38(*anti*) were measured from PDB 420D (ref. ⁴⁰) and 157D (ref. ⁴¹), respectively. **b**, 'H-'H NOESY and ¹⁵N-'H HSQC spectra of the exchangeable imino/amino proton region of preE-miR-21 in H₂O at 10 °C and pH 4.35. **c**, 'H-'H NOESY and ¹³C-'H HSQC spectra of the nonexchangeable base proton region of preE-miR-21 in D₂O at 35 °C and pH 4.35. **d**, 'H-'H NOESY spectrum of the nonexchangeable base/sugar proton region of preE-miR-21 in D₂O at 35 °C and pH 4.35.

C2 and C8 of A22 can be attributed to protonation-induced major chemical-shift perturbations in the wild type, which cannot be recapitulated with this mutation. However, the deviations for C32-C5 and U36-C1' could be due to their relatively small chemical-shift differences (<0.5 ppm) and/or local conformational perturbations in the wild type from the mutation, which is the subject of future investigation. As the G38U mutant closely mimics the ES, it also provides some insights into the two residues (U24 and U26) in the pre-element region that showed no detectable RD. For U24-C6, its flat RD profile can be explained with essentially identical chemical shifts between the ground and excited states, as indicated with $\Delta \varpi_{\rm G38U} \approx 0$, whereas the lack of detectable RD for U26-C6 may be due to additional local conformational perturbations that are the subject of further studies (Extended Data Fig. 9). To provide independent validation of the chemical-shift fingerprints of the ES, we compared $\Delta \varpi_{\rm G38II}$ to chemical-shift differences of the wild type between pH 8.04 and pH 4.81 ($\Delta \varpi_{pH}$), where the low pH value was chosen to shift the population towards the protonated ES without inducing global protonation of adenines and cytosines. Good agreement was observed between $\Delta\varpi_{\rm RD}$ and $\Delta\varpi_{\rm pH}$, except for some major deviations from unpaired adenines and cytosines that are likely due to rapid protonation at pH 4.81 given their intrinsic p $K_{\rm a}$ values (~3.5–4.2)³⁶ when unpaired (Fig. 3f and Extended Data Figs. 3 and 4). In particular, excellent agreement between $\Delta\varpi_{\rm RD}$ and $\Delta\varpi_{\rm pH}$ of A22-C2 and A22-C8 complements the G38U mutant. Taken together, these chemical-shift fingerprints of low pH and G38U are each able to recapitulate a portion of the ES structure, with low pH chemical shifts matching changes in A22 residues, and G38U chemical shifts matching throughout the rest of the structure.

To this end, we obtained direct support for the proposed ES secondary structure by carrying out NMR NOESY experiments of wild-type preE-miR-21 at pH 4.35, which shifts the GS↔ES equilibrium further towards predominantly the protonated ES state (Figs. 2f and 4). NOE cross-peaks between A22-H61/H62 to neighboring G21-H1 and G37-H1 in the two-dimensional (2D) ¹H-¹H NOESY spectrum of exchangeable imino/amino protons suggest that the

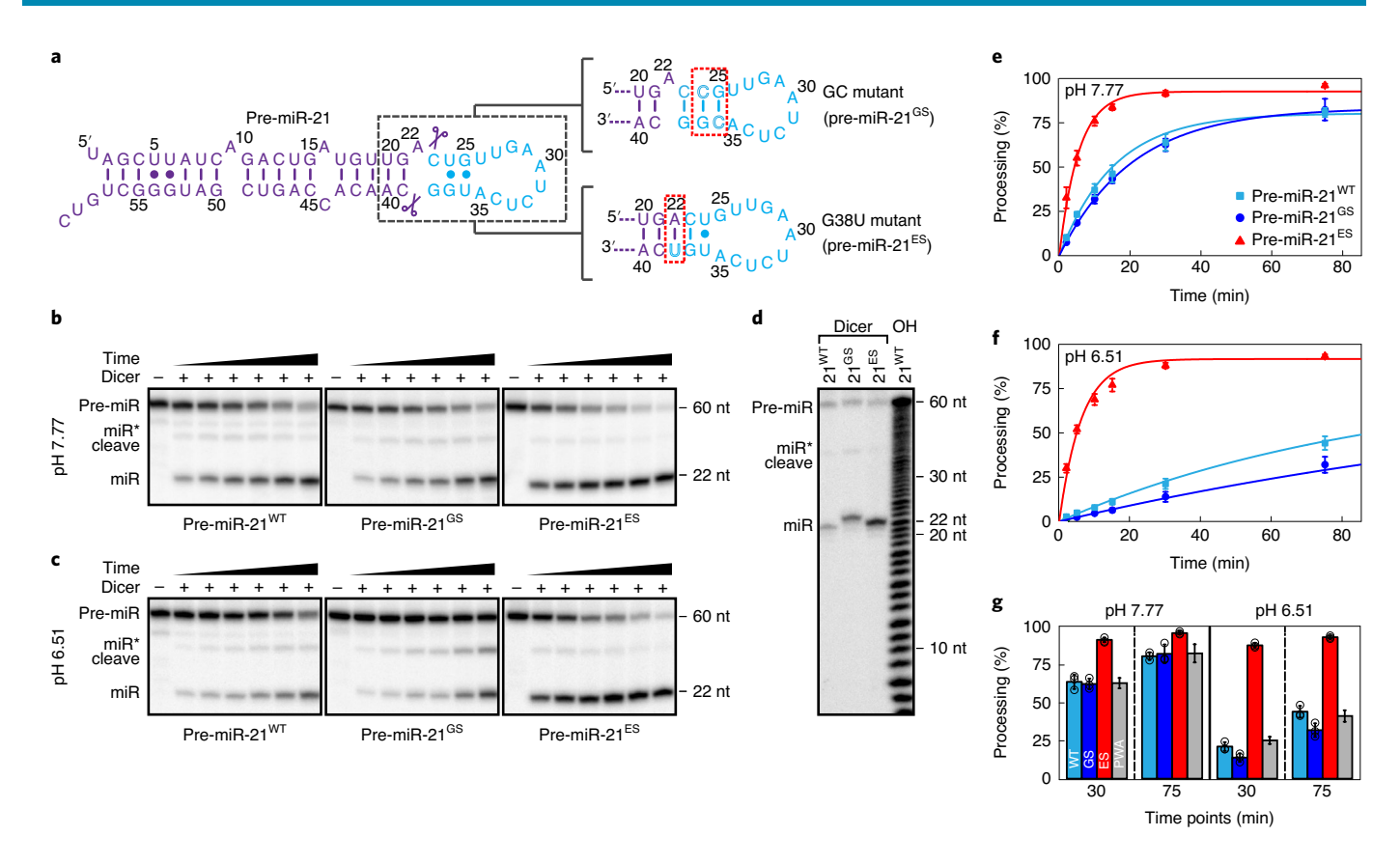


Fig. 5 | Excited state of preE-miR-21 enhances Dicer processing. a, Secondary structures of the wild type, ground-state mimic and excited-state mimic of pre-miR-21. **b,c**, Single-turnover processing assays of recombinant human Dicer (500 nM) with wild-type and mutant pre-miR-21s (2 nM) at pH 7.77 (**b**) and pH 6.51 (**c**) at 35 °C. **d**, Identification of cleavage products of wild-type and mutant pre-miR-21s using sequencing gel, where the RNA ladder is generated using alkaline hydrolysis of wild-type pre-miR-21. nt, nucleotide. **e,f**, Quantification of time-dependent Dicer processing of wild-type and mutant pre-miR-21s at pH 7.77 (**e**) and pH 6.51 (**f**) using ImageQuant. Solid lines represent best fits to a single exponential equation as described in the Methods. **g**, Histogram plots of the percentage of maturation of wild-type and mutant pre-miR-21s at 30-min and 75-min time points at pH 7.77 and 6.51. The population-weighted average of maturation is calculated on the basis of GS/ES populations at each pH condition and their corresponding processing percentages at each time point, as described in the Methods. Shown are the mean values and standard deviations (s.d.) from n = 3 independent assays.

protonated A22 is base paired and flanked by G21-C39 and C23-G37 base pairs (Fig. 4b). The imino/amino ¹H-¹H NOESY data further unveiled another ES secondary structural feature, in which U24 and U36 form the terminal base pair of the helical stem that encapsulates the protonated A22 (Fig. 4b). The presence of the U24-U36 base pair is also consistent with the exchangeable NOESY data of the ES-mimicking G38U mutant at regular pH 6.45 (Extended Data Fig. 9b). Next, we obtained the ¹H-¹H NOESY spectrum of nonexchangeable protons of wild-type preE-miR-21 at pH 4.35 (Fig. 4c,d), in which NOE cross-peaks between A22-H2 and G38-H8 strongly suggest that A22 and G38 are in the A22+(anti)-G38(syn) configuration (Fig. 4c). Furthermore, the A22+(anti) conformation is consistent with NOE cross-peaks between A22-H2 and the cross-strand residue C39-H1'; the G38(syn) conformation is supported with NOE cross-peaks between G38-H8 and the (n+1) residue C39-H1', whereas an G38(anti) conformation would result in NOE cross-peaks between G38-H8 and the (n-1) residue G37-H1', which are not detected in our experiment (Fig. 4d). Hence, these results strongly suggest that pre-miR-21 undergoes a global structural reshuffling at the pre-element region, where A22 is transiently protonated and forms a distinct $A^+(anti)$ -G(syn) base pair in the ES.

Pre-miR-21 encodes differential Dicer activities. To examine how the protonation-dependent structural changes may affect Dicer cleavage, we designed GS- and ES-mimicking substrates and per-

formed time-dependent Dicer processing assays42 at both acidic pH (6.45) and basic pH (7.77), where excess purified recombinant human Dicer was added to ensure single-turnover conditions (Fig. 5a and Extended Data Fig. 10). It is worth noting that while Dicer-binding protein TRBP can influence Dicer processing, since TRBP was shown not to affect cleavage of pre-miR-21 in vitro⁴², we only used recombinant Dicer in the assays to specifically evaluate the fitness of different substrate states. For the GS-mimicking substrate (pre-miR-21^{GS}), we mutated the two G•U wobbles with two G-C pairs, which was shown to stabilize the flexible stem that forms in the GS. For the ES-mimicking structure (pre-miR-21^{ES}), we incorporated a G38U mutation to the full-length pre-miR-21. We would like to note that the G38U mutant, which recapitulates key ES structural features, cannot perfectly mimic the electrostatic property of the protonated ES. However, since Dicer cleaves the phosphate backbone, we anticipate that structures of the backbone, rather than the base-pairing identity of the ES, may influence Dicer activity. Remarkably, GS- and ES-mimicking substrates exhibited substantially different Dicer activities (Fig. 5b-g). As can be seen, pre-miR-21^{ES} is robustly processed by Dicer at both pH conditions with an apparent rate of cleavage $(k_{\rm obs})$ being $2.7 \pm 0.3 \times 10^{-3} \,\rm s^{-1}$ at pH 6.51 and $3.0 \pm 0.3 \times 10^{-3}$ s⁻¹ at pH 7.77 (Fig. 5b,e). This observation is consistent with a previous study showing that Dicer can readily process double-stranded RNA (dsRNA) substrates over a pH range of 6.2-8.5 (ref. 43). In contrast, pre-miR-21GS is not

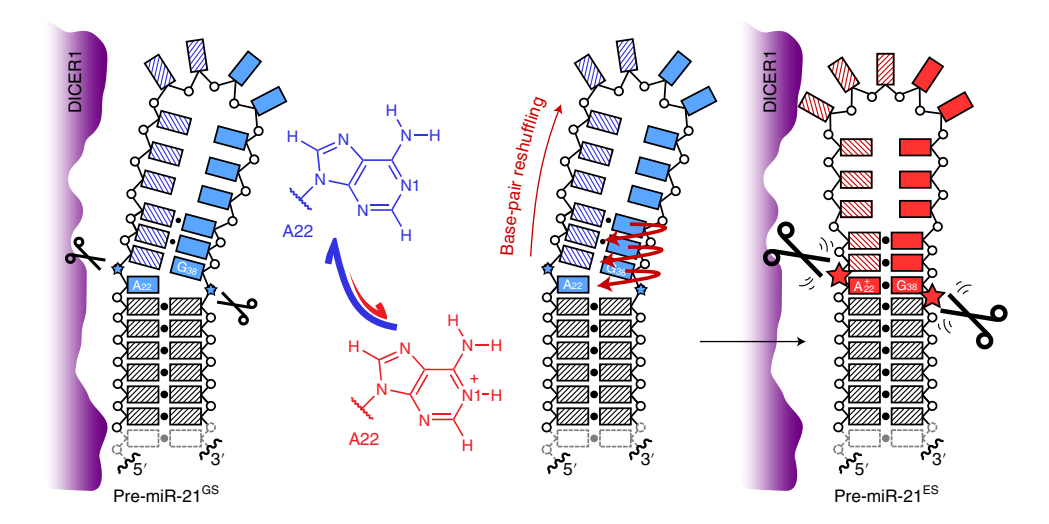


Fig. 6 | Modulation of miR-21 maturation with a protonation-dependent structural ensemble. Protonation at the N1 site of A22 sequesters the bulged adenine into a noncanonical A+-G mismatch and is associated with a long-range conformational reshuffling of the pre-element region. This structural rearrangement results in a conformation that is better suited for Dicer processing to generate mature miR-21.

only processed much less efficiently, but also displays a strong pH dependence, with $k_{\rm obs}$ changing from $9.5 \pm 0.4 \times 10^{-5} \, \rm s^{-1}$ at pH 6.51 to $8.1 \pm 0.4 \times 10^{-4}$ s⁻¹ at pH 7.77 (Fig. 5c,f), the mechanism of which is of interest for future investigations. By encapsulating dsRNA cleavage sites, pre-miR-21^{ES} represents a better substrate for Dicer over pre-miR-21^{GS}, with an approximately 4-28-fold enhancement in the observed cleavage rate. Moreover, while the double-stranded geometry of pre-miR-21^{ES} allows it to maintain the same cleavage site of A22 as the wild type, the stem-bulge-stem conformation of pre-miR-21^{GS} around the cleavage site, which was stabilized upon mutating the flexible G•U wobbles to G-C pairs, shifts the cleavage site by one nucleotide to C23 (Fig. 5d). This observation also agrees with a recent study showing a shifted cleavage site upon stabilizing a stem-bulge-stem conformation within the helical region of pre-miRNA upon mutation¹⁹. Hence, these results indicate that a weak GS apical stem may play an important role in accurate miR-21 maturation. Interestingly, relative to pre-miR-21^{GS} and pre-miR-21^{ES}, the wild-type (WT) substrate (pre-miR-21^{WT}) is processed at intermediate efficiencies, with $k_{\rm obs}$ being $1.8 \pm 0.1 \times 10^{-4} \, \rm s^{-1}$ and $1.1 \pm 0.1 \times 10^{-3} \text{ s}^{-1}$ at pH 6.51 and 7.77, respectively (Fig. 5b-f). Since pre-miR-21^{WT} undergoes pH-dependent GS↔ES equilibrium, we further evaluated whether its apparent processing efficiency could result from a dynamic average of the two conformational states. Indeed, the population-weighted average of Dicer cleavages of pre-miR-21^{GS} and pre-miR-21^{ES} closely resembles the overall maturation of pre-miR-21WT at different time points and different pH conditions (Fig. 5g), suggesting that Dicer processes pre-miR-21WT as an equilibrated dynamic ensemble. Together, these results not only unveil differential fitness of the GS and ES of the pre-element region of the pre-miR-21 for miR-21 maturation, but also further exemplify the importance of RNA structures in directing the overall outcome of miRNA biogenesis.

Discussion

Here, by integrating structural, dynamic and functional analyses of the miR-21 precursor, we showed that the intrinsic conformational plasticity of miRNA-processing intermediates can serve as a new layer of regulation for miRNA biogenesis. Often, structural changes in pri-/pre-miRNAs can be induced upon binding to protein regulators¹⁵, nucleotide modification, such as ADAR1-mediated adenine-to-inosine editing¹⁶ and METTL1-mediated methylation¹⁷, and disease-linked mutations¹⁸. RNA structural motifs are also important factors in recognition by processing machineries

for miRNA biogenesis, where altering primary and/or precursor structures of a target miRNA can further lead to altered biogenesis, inducing a change in physiological outcomes³. In contrast to these adaptive changes, we found that pre-miR-21 encodes a dynamic ensemble in its apical stem-loop region that undergoes spontaneous structural transitions between two kinetically and functionally distinct states (Fig. 6). In the GS, the two Dicer cleavage sites reside within a largely unstructured region; in contrast, both locations become structured in the ES. Relative to the GS, the ES conformation closely resembles the optimal substrate structure for Dicer, where both cleavage sites reside within a double-stranded helix and are positioned two nucleotides away from a flexible apical loop¹³, providing a better topology for Dicer cleavage.

A hallmark of the ES of pre-miR-21 is protonation of the adenine residue at the Dicer cleavage site. Protonation is a fundamental chemical property and one of the smallest chemical modifications on nucleic acids³⁶. The intrinsic pK_a values for protonation of adenines and cytosines are acidic and reside far from physiological pH ranges. However, by adopting sophisticated structures, RNA can shift acidic pK_a values toward neutral pHs to achieve specific ionization under physiological conditions for function³⁶. For example, the universally conserved adenine at the ribosome active site has a shifted pK_a to serve as a general acid-base catalyst for peptide formation⁴⁴, whereas the murine leukemia virus recoding signal employs a protonated adenine to structurally stabilize a compact pseudoknot to allow the ribosome to bypass the Gag stop codon³³. Here, protonation provides the crucial chemical basis for pre-miR-21 to form the A⁺(anti)-G(syn) base pair, which ensures the cleavage site adopts an overall A-form-like topology in the ES. Notably, the $A22^{+}(anti)$ -G(syn) base pair can be further stabilized through stacking interactions with consecutive C23-G37 and U24-U36 base pairs, a structural feature also observed in protonated HIV-1 RRE RNA34, which may contribute to the shifted pK_a of A22. Without being protonated, the adenine residue may still be able to pair with the upper stem guanine residue, albeit in the form of an A(anti)-G(anti) mismatch, which is likely functionally indistinguishable from the GS. Another feature of pre-miR-21 protonation is that the underlying structural transition occurs on the millisecond timescale, which is substantially faster than those involved in major structural changes, such as the adenine protonation in murine leukemia virus³³. This fast GS↔ES interconversion could enable pre-miR-21 to rapidly reach a new equilibrium upon a transient high acid load due to disease-induced metabolic shifts, thus modulating maturation of

miR-21 in response to environmental stimuli. Despite displaying distinct in vitro outcomes, a functional understanding of the role of pre-miR-21 protonation in regulating biogenesis will require future investigations that evaluate the response of pre-miR-21 under various cellular conditions, such as hypoxia and acidosis, as well as the effects of TRBP under these cellular conditions.

Interestingly, the spontaneous conformational transition in pre-miR-21 is reminiscent of that observed in Lin28-dependent regulation of the biogenesis of the let-7 family of miRNAs⁴⁵. In general, RNA secondary structural changes encounter large kinetic barriers, and hence need to be catalyzed by external factors, such as RNA-binding proteins like Lin28. In contrast, pre-miR-21 accomplishes such structural changes without protein factors, by accessing an ES. Here, all structural elements of the apical stem-loop—the bulge, metastable stem and flexible loop—are essential to achieve this concerted movement, and eliminating any of them abolishes the spontaneous transitions, exemplifying an ES-based mechanism for remodeling distant motifs that has also been recently reported in HIV-1 TAR RNA³⁸. Since the apical stem-loop is a common structural feature among all pri-/pre-miRNAs, we speculate that many miRNA-processing intermediates may encode similar ES-based conformational plasticity for long-range communication across their regulatory pre-element regions, which is further supported by a recent computational modeling of secondary structural ensembles of miRNAs18.

It has become increasingly clear that many noncoding RNAs do not fold into single static structures; instead, they dynamically interconvert between different conformational states for function²⁰. Recent developments in NMR techniques have opened up new avenues to probe RNA structural transitions involving alternative conformational states that often evade detection from conventional biophysical and biochemical methods due to their low populations and/or transient lifetimes^{31,32,37}. In particular, the development of our nucleic acid-optimized ¹⁵N NMR CEST method has enabled direct identification of transient protonation in nucleic acids, illuminating the crucial chemical basis for delineating the relationship between structure and function. With the emerging view of ESs as a 'hidden' layer of regulation²⁰, the growing repertoire of functional RNA ESs with distinct structural features promise new strategies and developments in RNA-targeted therapeutics.

Online content

Any methods, additional references, Nature Research reporting summaries, source data, extended data, supplementary information, acknowledgements, peer review information; details of author contributions and competing interests; and statements of data and code availability are available at https://doi.org/10.1038/s41589-020-00667-5.

Received: 22 November 2019; Accepted: 2 September 2020; Published online: 26 October 2020

References

- Friedman, R. C., Farh, K. K., Burge, C. B. & Bartel, D. P. Most mammalian mRNAs are conserved targets of microRNAs. *Genome Res.* 19, 92–105 (2009).
- Siomi, H. & Siomi, M. C. Posttranscriptional regulation of microRNA biogenesis in animals. *Mol. Cell* 38, 323–332 (2010).
- Ha, M. & Kim, V. N. Regulation of microRNA biogenesis. Nat. Rev. Mol. Cell Biol. 15, 509–524 (2014).
- Gebert, L. F. R. & MacRae, I. J. Regulation of microRNA function in animals. Nat. Rev. Mol. Cell Biol. 20, 21–37 (2019).
- Treiber, T., Treiber, N. & Meister, G. Regulation of microRNA biogenesis and its crosstalk with other cellular pathways. *Nat. Rev. Mol. Cell Biol.* 20, 5–20 (2019).
- Esteller, M. Non-coding RNAs in human disease. *Nat. Rev. Genet.* 12, 861–874 (2011).
- Lin, S. & Gregory, R. I. MicroRNA biogenesis pathways in cancer. Nat. Rev. Cancer 15, 321–333 (2015).

8. Zhang, X. & Zeng, Y. The terminal loop region controls microRNA processing by Drosha and Dicer. *Nucleic Acids Res.* **38**, 7689–7697 (2010).

- Tsutsumi, A., Kawamata, T., Izumi, N., Seitz, H. & Tomari, Y. Recognition of the pre-miRNA structure by *Drosophila Dicer-1*. *Nat. Struct. Mol. Biol.* 18, 1153–1158 (2011).
- Castilla-Llorente, V., Nicastro, G. & Ramos, A. Terminal loop-mediated regulation of miRNA biogenesis: selectivity and mechanisms. *Biochem. Soc. Trans.* 41, 861–865 (2013).
- Auyeung, V. C., Ulitsky, I., McGeary, S. E. & Bartel, D. P. Beyond secondary structure: primary-sequence determinants license pri-miRNA hairpins for processing. *Cell* 152, 844–858 (2013).
- Nguyen, T. A., Park, J., Dang, T. L., Choi, Y. G. & Kim, V. N. Microprocessor depends on hemin to recognize the apical loop of primary microRNA. *Nucleic Acids Res.* 46, 5726–5736 (2018).
- 13. Gu, S. et al. The loop position of shRNAs and pre-miRNAs is critical for the accuracy of dicer processing in vivo. *Cell* **151**, 900–911 (2012).
- Contrant, M. et al. Importance of the RNA secondary structure for the relative accumulation of clustered viral microRNAs. *Nucleic Acids Res.* 42, 7981–7996 (2014).
- van Kouwenhove, M., Kedde, M. & Agami, R. MicroRNA regulation by RNA-binding proteins and its implications for cancer. *Nat. Rev. Cancer* 11, 644–656 (2011).
- Liu, Z., Wang, J., Li, G. & Wang, H. W. Structure of precursor microRNA's terminal loop regulates human Dicer's dicing activity by switching DExH/D domain. *Protein Cell* 6, 185–193 (2015).
- Pandolfini, L. et al. METTL1 promotes let-7 microRNA processing via m7G methylation. Mol. Cell 74, 1278–1290 (2019).
- Dallaire, P. et al. Structural dynamics control the microRNA maturation pathway. Nucleic Acids Res. 44, 9956–9964 (2016).
- Iki, T. et al. Structural flexibility enables alternative maturation, ARGONAUTE sorting and activities of miR168, a global gene silencing regulator in plants. *Mol. Plant* 11, 1008–1023 (2018).
- Ganser, L. R., Kelly, M. L., Herschlag, D. & Al-Hashimi, H. M. The roles of structural dynamics in the cellular functions of RNAs. *Nat. Rev. Mol. Cell Biol.* 20, 474–489 (2019).
- Zeng, Y. & Cullen, B. R. Sequence requirements for micro RNA processing and function in human cells. RNA 9, 112–123 (2003).
- 22. Volinia, S. et al. A microRNA expression signature of human solid tumors defines cancer gene targets. *Proc. Natl Acad. Sci. USA* 103, 2257–2261 (2006).
- Kumarswamy, R., Volkmann, I. & Thum, T. Regulation and function of miRNA-21 in health and disease. RNA Biol. 8, 706–713 (2011).
- Zeng, Y., Yi, R. & Cullen, B. R. Recognition and cleavage of primary microRNA precursors by the nuclear processing enzyme Drosha. EMBO J. 24. 138–148 (2005).
- Trabucchi, M. et al. The RNA-binding protein KSRP promotes the biogenesis of a subset of microRNAs. Nature 459, 1010–1014 (2009).
- Chirayil, S., Wu, Q., Amezcua, C. & Luebke, K. J. NMR characterization of an oligonucleotide model of the miR-21 pre-element. PLoS ONE 9, e108231 (2014).
- Shortridge, M. D. et al. A macrocyclic peptide ligand binds the oncogenic microRNA-21 precursor and suppresses Dicer processing. ACS Chem. Biol. 12, 1611–1620 (2017).
- Massi, F., Johnson, E., Wang, C., Rance, M. & Palmer, A. G. 3rd NMR R1rho rotating-frame relaxation with weak radio frequency fields. *J. Am. Chem. Soc.* 126, 2247–2256 (2004).
- Korzhnev, D. M., Orekhov, V. Y. & Kay, L. E. Off-resonance R_{1p} NMR studies of exchange dynamics in proteins with low spin-lock fields: an application to a Fyn SH3 domain. *J. Am. Chem. Soc.* 127, 713–721 (2005).
- Hansen, A. L., Nikolova, E. N., Casiano-Negroni, A. & Al-Hashimi, H. M. Extending the range of microsecond-to-millisecond chemical exchange detected in labeled and unlabeled nucleic acids by selective carbon R_{1p} NMR spectroscopy. J. Am. Chem. Soc. 131, 3818–3819 (2009).
- Sekhar, A. & Kay, L. E. NMR paves the way for atomic level descriptions of sparsely populated, transiently formed biomolecular conformers. *Proc. Natl Acad. Sci. USA* 110, 12867–12874 (2013).
- 32. Palmer, A. G. 3rd Chemical exchange in biomacromolecules: past, present, and future. *J. Magn. Reson.* **241**, 3–17 (2014).
- Houck-Loomis, B. et al. An equilibrium-dependent retroviral mRNA switch regulates translational recoding. *Nature* 480, 561–564 (2011).
- Chu, C. C., Plangger, R., Kreutz, C. & Al-Hashimi, H. M. Dynamic ensemble of HIV-1 RRE stem IIB reveals non-native conformations that disrupt the Rev-binding site. *Nucleic Acids Res.* 47, 7105–7117 (2019).
- Zhao, B., Baisden, J. T. & Zhang, Q. Probing excited conformational states of nucleic acids by nitrogen CEST NMR spectroscopy. J. Magn. Reson. 310, 106642 (2020).
- Thaplyal, P. & Bevilacqua, P. C. Experimental approaches for measuring pK_a's in RNA and DNA. Methods Enzymol. 549, 189–219 (2014).
- Dethoff, E. A., Petzold, K., Chugh, J., Casiano-Negroni, A. & Al-Hashimi, H. M. Visualizing transient low-populated structures of RNA. *Nature* 491, 724–728 (2012).

- Lee, J., Dethoff, E. A. & Al-Hashimi, H. M. Invisible RNA state dynamically couples distant motifs. Proc. Natl Acad. Sci. USA 111, 9485–9490 (2014).
- Parisien, M. & Major, F. The MC-Fold and MC-Sym pipeline infers RNA structure from sequence data. *Nature* 452, 51–55 (2008).
- Pan, B., Mitra, S. N. & Sundaralingam, M. Crystal structure of an RNA 16-mer duplex R(GCAGAGUUAAAUCUGC)₂ with nonadjacent G(syn)·A⁺(anti) mispairs. *Biochemistry* 38, 2826–2831 (1999).
- 41. Leonard, G. A. et al. Crystal and molecular structure of r(CGCGAAUUAGCG): an RNA duplex containing two G(anti)·A(anti) base pairs. *Structure* **2**, 483–494 (1994).
- Lee, H. Y. & Doudna, J. A. TRBP alters human precursor microRNA processing in vitro. RNA 18, 2012–2019 (2012).
- Zhang, H., Kolb, F. A., Brondani, V., Billy, E. & Filipowicz, W. Human Dicer preferentially cleaves dsRNAs at their termini without a requirement for ATP. EMBO J. 21, 5875–5885 (2002).
- 44. Muth, G. W., Ortoleva-Donnelly, L. & Strobel, S. A. A single adenosine with a neutral pK_a in the ribosomal peptidyl transferase center. *Science* **289**, 947–950 (2000)
- Nam, Y., Chen, C., Gregory, R. I., Chou, J. J. & Sliz, P. Molecular basis for interaction of let-7 microRNAs with Lin28. Cell 147, 1080–1091 (2011).

Publisher's note Springer Nature remains neutral with regard to jurisdictional claims in published maps and institutional affiliations.

© The Author(s), under exclusive licence to Springer Nature America, Inc. 2020

Methods

Sample preparation. Unlabeled, uniformly $^{13}\text{C}/^{15}\text{N}$ -labeled and adenine-specifically $^{13}\text{C}/^{15}\text{N}$ -labeled preE-miR-21 samples and mutants were prepared as previously described*6 Briefly, after in vitro transcription, samples were ethanol precipitated, gel purified using 15% denaturing polyacrylamide gel, electroeluted with the Elutrap system (Whatman), purified with an 5-ml Hi-Trap Q anion-exchange column (GE Healthcare) and desalted by exchanging into H₂O using an Amicon filtration unit with a 3-kDa molecular weight cut-off membrane (Millipore). Samples were then concentrated and exchanged into NMR buffers with 50 mM KCl and $50\,\mu\text{M}$ EDTA, where $10\,\text{mM}$ acetate buffers were used for pH at 4.35, 4.96 and 5.41, and $10\,\text{mM}$ sodium phosphate buffers were used for pH at 5.98, 6.45, 6.96, 7.47 and 8.04. For H₂O samples, 5% D₂O was added. For D₂O samples in sodium phosphate buffer, H₂O samples were lyophilized and redissolved in the same volume of 99.996% D₂O (Sigma). For D₂O samples in sodium acetate buffer, samples were exchanged into 10 mM acetate buffer with 50 mM KCl and 50 μM EDTA in D₂O.

NMR spectroscopy. All NMR experiments were carried out on a Bruker Avance III 600 MHz spectrometer equipped with a 5-mm triple resonance (TCI) cryogenic probe. Exchangeable proton spectra were recorded using H_2O samples at 283 K, and nonexchangeable proton spectra were recorded at 298 K and 308 K using H_2O and D_2O samples. Spectra were processed and analyzed with TOPSPIN 3.5 (Bruker), NMRPipe⁴⁷, NMRView⁴⁸ and Sparky v.3.110 (University of California, San Franscisco). The assignments for preE-miR-21 were obtained with samples at pH 6.45 and 8.04 and the assignments for its mutants were obtained with samples at pH 6.45 using 2D NOESY, 2D TOCSY, $^{1}H_{-}^{13}N$ HSQC, $^{1}H_{-}^{13}C$ HSQC, 2D HCCH-COSY and HCN experiments on unlabeled, uniformly labeled and adenine-specifically $^{13}C/^{15}N$ -labeled samples with standard protocols⁴⁹. The apparent pK_a values of adenines were obtained by fitting the pH-dependent excited-state population and chemical shift to the Henderson–Hasselbalch equation as described previously⁵⁰.

 13 C R_{10} relaxation dispersion measurements and data analysis. The on- and off-resonance relaxation dispersion profiles were measured at 308 K using the one-dimensional (1D) selective R_{10} experiment developed by Al-Hashimi and co-workers³⁰ and a constant-time approach described by Kay and co-workers²⁹, where R_{10} values were obtained from a single delay period (T_{EX}). For on-resonance experiments, the relaxation delay was set to $T_{\rm EX} = 32 \, \text{ms}$; for off-resonance experiments, the relaxation delay was set to $T_{\rm EX}=40$ ms, except $T_{\rm EX}=16$ ms for A22-C8 and A35-C1' and $T_{\rm EX}=24$ ms for C23-C6, U36-C6, and G28-C1'. Relaxation rates were determined by fitting peak intensity to a single exponential decay as $R_{10} = -\ln(I_T/I_0)/T_{EX}$, where I_T is the decayed peak intensity and I_0 is the reference peak intensity. Relaxation rate errors were estimated by intensity deviations between three duplicates at $T_{\rm EX}$ = 0 and the signal-to-noise ratios in 1D spectra. The largest of the two errors was reported. For on-resonance experiments, eleven ¹³C spin-lock fields ($\omega/2\pi$) of 100, 199 (×2), 299, 399, 498 (×2), 786, 982, 1,474, 1,965 (×2), 2,456 and 2,947 Hz were employed, (×2) indicates performed in duplicate. Due to large C–C couplings, the lowest 13 C spin-lock field ($\omega/2\pi$) of 100 Hz was not used in measuring on-resonance C5/C6/C1' RD profiles. For off-resonance experiments, three 13 C spin-lock fields ($\omega/2\pi$) of 299, 498 and 786 Hz were used. For $\omega/2\pi = 299$ Hz, the ¹³C offsets ranged between -600 and 600 Hz with a spacing of 100 Hz and a smaller spacing of 50 Hz between -200 and 200 Hz; for $\omega/2\pi = 498$ Hz, the ¹³C offsets ranged between -1,000 and 1,000 Hz with a spacing of 200 Hz from -1,000 to -800 Hz and from 800 to 1,000 Hz, a spacing of 100 Hz from -800 to -100 Hz and from 100 to 800 Hz, and single points at -50 and 50 Hz; for $\omega/2\pi = 786$ Hz, the ¹³C offsets ranged between -2,000 and 2,000 Hz with a spacing of 500 Hz from −2,000 to −1,000 Hz and 1,000 to 2,000 Hz, a spacing of 250 Hz from -1,000 to -500 Hz and 500 to 1,000 Hz, and a spacing of 100 Hz from -500 to -100 Hz and from 100 to 500 Hz, and single points at -50 and 50 Hz. 13 C spin-lock powers were calibrated according to the 1D approach by Guenneugues et al.51 as previously described46,52.

Relaxation dispersion profiles were analyzed as described previously 46 . Briefly, on- and off-resonance relaxation dispersion profiles were obtained by measuring the rate of decay of magnetization over the spin-lock period as a function of spin-lock power $(\omega_{\rm eff}/2\pi)$ and spin-lock offset (Ω) , respectively, where $\Omega=\omega_{\rm rf}-\Omega_{\rm obs}$ is the frequency difference between the spin-lock carrier frequency $(\omega_{\rm rf})$ and the observed resonance frequency $(\Omega_{\rm obs})$. The $R_{\rm 1p}$ profiles of residues displaying conformational exchange were fit to a two-state exchange model between the ground (G) and excited (E) states based on the Bloch–McConnell equation 53 ,

$$\frac{\mathrm{d}}{\mathrm{d}t} \begin{pmatrix} I_{\mathrm{g}}^{\mathrm{G}} \\ I_{\mathrm{g}}^{\mathrm{G}} \\ I_{\mathrm{g}}^{\mathrm{G}} \\ I_{\mathrm{g}}^{\mathrm{G}} \\ I_{\mathrm{g}}^{\mathrm{E}} \end{pmatrix} =$$

$$\begin{pmatrix} -R_{2}^{\mathrm{G}} - k_{\mathrm{GE}} & -\omega_{\mathrm{G}} & 0 & 0 & 0 \\ \omega_{\mathrm{G}} & -R_{2}^{\mathrm{G}} - k_{\mathrm{GE}} & -\omega_{\mathrm{1}} & 0 & k_{\mathrm{EG}} & 0 & 0 \\ 0 & \omega_{\mathrm{1}} & -R_{\mathrm{1}}^{\mathrm{G}} - k_{\mathrm{GE}} & 0 & 0 & k_{\mathrm{EG}} & 0 \\ 0 & \omega_{\mathrm{1}} & -R_{\mathrm{1}}^{\mathrm{G}} - k_{\mathrm{GE}} & 0 & 0 & k_{\mathrm{EG}} & 0 \\ 0 & k_{\mathrm{GE}} & 0 & 0 & -R_{2}^{\mathrm{E}} - k_{\mathrm{EG}} & -\omega_{\mathrm{E}} & 0 \\ 0 & k_{\mathrm{GE}} & 0 & \omega_{\mathrm{E}} & -R_{2}^{\mathrm{E}} - k_{\mathrm{EG}} & -\omega_{\mathrm{1}} \\ 0 & 0 & k_{\mathrm{GE}} & 0 & \omega_{\mathrm{1}} & -R_{1}^{\mathrm{E}} - k_{\mathrm{EG}} \end{pmatrix}$$

where $R_1^{\text{G/E}}$ is the longitudinal relaxation rate of the ground/excited state, $R_2^{\text{G/E}}$ is the transverse relaxation rate of the ground/excited state, $\omega_{G/E}$ is the offset of the applied ¹³C spin lock with a strength of ω_1 from the chemical shift ($\Omega_{G/E}$) of the ground/excited state and $k_{\rm GE}$ and $k_{\rm EG}$ are forward and backward exchange rates as defined by $k_{GE} = p_E k_{ex}$ and $k_{EG} = p_G k_{ex}$. Here, $k_{ex} = k_{GE} + k_{EG}$ is the rate of exchange, p_G and p_E are populations of ground and excited states, respectively, and $\Omega_{\rm obs} = p_{\rm G}\Omega_{\rm G} + p_{\rm E}\Omega_{\rm E}$ and $\Omega_{\rm E} = \Omega_{\rm G} + \Delta\omega$, where $\Delta\omega$ is the chemical shift difference between the ground and excited states. Ground-state and excited-state magnetizations at the beginning of the $T_{\rm EX}$ period are along the effective spin-lock field as, $I_x^{\text{G/E}} = p_{\text{G/E}} \sin(\theta)$, $I_y^{\text{G/E}} = 0$, $I_z^{\text{G/E}} = p_{\text{G/E}} \cos(\theta)$, where $\theta = \arctan(\omega_1/\Omega)$ is the effective tilt angle. Fitting parameters are $R_1 = R_1^{G/E}$, $R_2 = R_2^{G/E}$, $\Delta \omega$, $k_{\rm ex}$ and $p_{\rm E}$, where we assume $R_1^G = R_1^E$ and $R_2^G = R_2^E$. Since the applied ¹³C spin-lock powers are strong enough to decouple C-C couplings, the relaxation dispersion profiles of C1', C5 and C6 were analyzed the same as the C2 and C8 profiles. For global fitting of dispersion profiles at individual pH conditions, spin-specific R_1 , R_2 and $\Delta \omega$ were used, whereas $k_{\rm ex}$ and $p_{\rm F}$ were fit globally. For residues without conformational exchange, the two-state model was simplified to a one-state model by fixing all exchange parameters (rate of exchange $k_{\rm ex}$ and population of excited state $p_{\rm E}$) to 0. All profiles were fitted using an in-house OriginLab program with a Levenberg-Marquardt algorithm.

¹⁵N CEST measurements and data analysis. ¹⁵N CEST profiles were measured at 308 K using a recently developed $^2J_{\rm NH}$ -based 2D 1 H-¹⁵N HSQC CEST experiment pulse sequence that monitors longitudinal two-spin order (2N₂H₂) as described previously. ³⁵. The ¹⁵N carrier was set to 224.9 ppm with a spectral width of 6 ppm, and the range of ¹⁵N offsets was set to between -6,000 Hz and 3,000 Hz with a spacing of 200 Hz, except for a of spacing of 50 Hz from -4,200 to -3,800 Hz and from 600 to 1,000 Hz. With a relaxation period of $T_{\rm EX}$ =0.1 s, two ¹⁵N B_1 fields (ω /2 π) of 52.1 Hz and 104.7 Hz were used at pH 8.04 and one ¹⁵N B_1 field (ω /2 π) of 52.1 Hz was used at pH7.47 and 6.96. The 1D approach by Guenneugues et al. ⁵¹ was used to calibrate ¹⁵N spin-lock powers as previously described ^{46,52}. For all measurements, three spectra ($T_{\rm EX}$ =0 s) were recorded for reference in data fitting and error estimation.

CEST profiles were analyzed as described previously 15 . Briefly, CEST profiles were obtained by normalizing peak intensity relative to those at $T_{\rm EX}=0$ as a function of spin-lock offset (Ω) , where $\Omega=\omega_{\rm rf}-\Omega_{\rm obs}$ is the frequency difference between the spin-lock carrier frequency $(\omega_{\rm rf})$ and the observed resonance frequency $(\Omega_{\rm obs})$. Errors in CEST measurements were estimated on the basis of both triplicates at $T_{\rm EX}=0$ s and the baseline of profiles. The 15 N CEST profiles of A22-N1 at various pH values displaying conformational exchange were fit to a two-state exchange model between the ground (G) and excited (E) states based on the Bloch–McConnell equation 53 of a coupled two-spin 15 N- 1 H system $^{54.55}$,

$$\frac{\mathrm{d}}{\mathrm{d}t}\mathbf{v}^{\frac{G}{\mathrm{E}}} = -\mathbf{R}^{\frac{G}{\mathrm{E}}}\mathbf{v}^{\frac{G}{\mathrm{E}}} = \begin{pmatrix} R_{2}^{\frac{G}{\mathrm{E}}} & \omega_{\mathrm{K}}^{\frac{G}{\mathrm{E}}} & 0 & \eta_{\mathrm{X}y}^{\frac{G}{\mathrm{E}}} & \pi J_{\mathrm{NH}}^{\frac{G}{\mathrm{E}}} & 0 \\ -\omega_{\mathrm{K}}^{\frac{G}{\mathrm{E}}} & R_{2}^{\frac{G}{\mathrm{E}}} & \omega_{1} & -\pi J_{\mathrm{NH}}^{\frac{G}{\mathrm{E}}} & \eta_{\mathrm{X}y}^{\frac{G}{\mathrm{E}}} & 0 \\ 0 & -\omega_{1} & R_{1}^{\frac{G}{\mathrm{E}}} & 0 & 0 & \eta_{z}^{\frac{G}{\mathrm{E}}} \\ \eta_{\mathrm{X}y}^{\frac{G}{\mathrm{E}}} & \pi J_{\mathrm{NH}}^{\frac{G}{\mathrm{E}}} & 0 & R_{2}^{\frac{G}{\mathrm{E}}} & \omega_{\mathrm{K}}^{\frac{G}{\mathrm{E}}} & 0 \\ -\pi J_{\mathrm{NH}}^{\frac{G}{\mathrm{E}}} & \eta_{\mathrm{X}y}^{\frac{G}{\mathrm{E}}} & 0 & -\omega_{\mathrm{N}}^{\frac{G}{\mathrm{E}}} & R_{2\mathrm{H}}^{\frac{G}{\mathrm{E}}} & \omega_{1} \\ 0 & 0 & 0 & \eta_{z}^{\frac{G}{\mathrm{E}}} & 0 & -\omega_{1} & R_{1}^{\frac{G}{\mathrm{E}}} \\ \end{pmatrix} \begin{pmatrix} \eta_{\mathrm{X}}^{\frac{G}{\mathrm{E}}} & \eta_{\mathrm{X}y}^{\frac{G}{\mathrm{E}}} & 0 \\ N_{\mathrm{X}}^{\frac{G}{\mathrm{E}}} & 2H_{2}N_{2}^{\frac{G}{\mathrm{E}}} & 2H_{2}N_{2}^{\frac{G}{\mathrm{E}}} \\ 2H_{2}N_{2}^{\frac{G}{\mathrm{E}}} & 2H_{2}N_{2}^{\frac{G}{\mathrm{E}}} \end{pmatrix}$$

$$\frac{\mathrm{d}}{\mathrm{d}t}\sigma(t) = -\mathbf{L} \begin{bmatrix} \mathbf{v^G} \\ \mathbf{v^E} \end{bmatrix} = \left(\begin{bmatrix} \mathbf{R^G} & \mathbf{0_6} \\ \mathbf{0_6} & \mathbf{R^E} \end{bmatrix} + \begin{bmatrix} -k_{\mathrm{GE}} & k_{\mathrm{EG}} \\ k_{\mathrm{GE}} & -k_{\mathrm{EG}} \end{bmatrix} \otimes \mathbf{1_6} \right) \begin{bmatrix} \mathbf{v^G} \\ \mathbf{v^E} \end{bmatrix}$$

where ${\bf v}^{\rm G/E}$ and ${\bf R}^{\rm G/E}$ are the ground/excited-state magnetization and relaxation matrices, respectively; $R_1^{\rm G/E}$ and $R_2^{\rm G/E}$ are the ground/excited state $^{15}{\rm N}$ longitudinal and transverse relaxation rates, respectively; $R_{\rm 1HN}^{\rm G/E}$ is the $^{15}{\rm N}^{\rm -1}{\rm H}$ two-spin order

relaxation rate of the ground/excited state; $R_{\rm 2HN}^{\rm G/E}$ is the $^{15}{\rm N}$ antiphase relaxation rate of the ground/excited state; $\eta_z^{\rm G/E}$ and $\eta_{xy}^{\rm G/E}$ are the N–H dipolar–dipolar/ nitrogen CSA cross-correlated relaxations between the ¹⁵N longitudinal and two-spin order elements and between ¹⁵N transverse and antiphase magnetizations, respectively; $\omega_N^{G/E}$ is the offset of the applied ¹⁵N spin-lock with a strength of ω_1 ; and $J_{\rm NH}^{\rm G/E}$ is the ¹⁵N-¹H scalar coupling of the ground/excited state. The $k_{\rm GE}$ and $k_{\rm EG}$ are forward and backward exchange rates as defined by $k_{GE} = p_E k_{ex}$ and $k_{EG} = p_G k_{ex}$. where $k_{\text{ex}} = k_{\text{GE}} + k_{\text{EG}}$ is the rate of exchange and p_{G} and p_{E} are populations of ground and excited states, respectively. Here, $\omega^G = \Omega_{obs}$ and $\omega^E = \omega^G + \Delta \omega$, where $\Delta \omega$ is the chemical shift difference between the ground and excited states. At the beginning of the T_{EX} period, GS and ES magnetizations are the two-spin order (2N_zH_z) along z and their populations are set to be at $p_{\rm G}$ and $p_{\rm E}$, respectively. The fitting parameters are $\Delta \omega$, $k_{\rm ex}$, $p_{\rm E}$, $R_{\rm E} = R_{\rm E}^{\rm G/E}$, $R_{\rm HN} = R_{\rm HN}^{\rm G/E}$ and $R_{\rm 2HN} = R_{\rm 2}^{\rm G/E} + R_{\rm HN}^{\rm G/E} - R_{\rm 1}^{\rm G/E}$ as described previously 35,56. In addition, $\eta_z^{\rm G/E}/\eta_{xy}^{\rm G/E}$ and $R_{\rm 1}^{\rm G/E}$ were set to 0 to simplify data fitting, where η_z/η_{xy} have been shown not to affect the extracted $\Delta\omega$, $k_{\rm ex}$ and $p_{\rm E}$ values^{35,57}, whereas the CEST data have been shown not to constrain determination of R_1 (ref. 35). For residues without conformational exchange, all exchange parameters (rate of exchange $k_{\rm ex}$ and population of excited state $p_{\rm E}$) were set to 0, which simplifies the two-state model to a one-state model. All profiles were fitted using an in-house OriginLab program with a Levenberg-Marquardt algorithm.

Preparation of Dicer substrates. Pre-miR-21 substrates were prepared by in vitro transcription, where a hammerhead ribozyme (HH) was fused to the 5' end of pre-miR-21s to generate 5'-OH substrates with wild-type 5' end nucleotide. During in vitro transcription, the hammerhead ribozyme self-cleaves, and the resulting miR-21 precursors are subsequently 5' end phosphorylated and labeled with $[\gamma^{-32}P]$ ATP. Sequences of the pre-miR-21 substrates were as follows:

HH-Pre-miR-21 WT: CUAAUACGACUCACUAUAGGAGCUACUGAUGAGGCCGAAAGGCCGAAACCCGAAAGGGUCUAGCUUAUCAGACUGAUGU-UGACUGUUGAAUCUCAUGGCAACACCAGUCGAUGGGCUGUC

HH-Pre-miR-21 GC mutant: CUAAUACGACUCACUAUAGGAGCUACUGA-UGAGGCCGAAAGGCCGAAACCCGAAAGGGUCUAGCUUAUCAGACUG-AUGUUGACCGUUGAAUCUCACGGCAACACCAGUCGAUGGGCUGUC

HH-Pre-miR-21 G38U mutant: CUAAUACGACUCACUAUAGGAGCUACUG AUGAGGCCGAAAGGCCGAAACCCGAAAGGGUCUAGCUUAUCAGACUGA UGUUGACUGUUGAAUCUCAUGUCAACACCAGUCGAUGGGCUGUC

After in vitro transcription, samples were exchanged into H_2O using Amicon filtration units (Millipore) with 10-kDa molecular weight cut-off membranes. The resulting substrates were subsequently subject to 5' end $^{32}\text{P-labeling}$ with T4 Polynucleotide Kinase (T4PNK) (New England Biolabs). A portion of $50\,\mu\text{l}$ of RNA at $400\,\text{nM}$ was incubated in a solution containing T4PNK buffer, $20\,\text{U}$ T4PNK and $[\gamma^{-32}\text{P}]\text{ATP}$ at $35\,^{\circ}\text{C}$ for $30\,\text{min}$ before being gel purified by 20% denaturing polyacrylamide gel. The $^{32}\text{P-labeled}$ RNAs were extracted from the gel by crushing and soaking in $250\,\text{mM}$ NaCl in $1\times$ TBE buffer for $24\,\text{h}$ before filtering and exchanging multiple times into H_2O using an Amicon filtration unit (Millipore) with a 10-kDa molecular wieght cut-off. The $^{32}\text{P-labeled}$ substrates were stored at $-20\,^{\circ}\text{C}$ before Dicer processing assay.

Preparation of recombinant human Dicer. Recombinant human Dicer was purified as described previously 58,59 , with minimal modifications. Specifically, 10^9 SF9 cells were infected with 10 muliplicity of infection of His-tagged Dicer baculovirus (a kind gift of B. Marzluff). After three days, cells were lysed in W100 buffer (20 mM Tris pH7.5, 100 mM NaCl, 1 mM MgCl $_2$, 5 mM β -mercaptoethanol, 10% glycerol, 0.5% Triton X100, protease inhibitors) and purified sequentially on Talon and NiNTA affinity resin. Purified enzyme was dialyzed against buffer W100 adjusted to 50% glycerol and stored at $-80\,^{\circ}\text{C}$. Activity was confirmed using a fluorescent-based cleavage assay.

Time-dependent single-turnover Dicer processing assay and data analysis.

The ³²P-labeled pre-miR-21 substrates were heated to 95 °C for 5 min and then placed on ice for 5 min to anneal the precursor hairpin. Substrate (4 µl) was mixed with $2\,\mu l$ of $5\times$ dicing buffer (120 mM HEPES at pH 7.77 or 120 mM Bis-Tris at pH 6.51, 0.5 M NaCl and 0.02 mM EDTA) and 2 µl of 25 mM MgCl₂. In a separate tube, concentrated recombinant human Dicer enzyme was diluted in 1× dicing buffer (24 mM HEPES or 24 mM Bis–Tris, 100 mM NaCl, $4\,\mu\text{M}$ EDTA) and mixed with an equal volume of 10 mM ATP. ATP/Dicer (2 µl) mixture (10 mM ATP and $0.2\,\mu l$ Dicer) was added to each tube of $8\,\mu l$ substrate mixture and incubated at 35 °C. The final concentrations of RNA substrates and Dicer were 2 nM and 500 nM, respectively, to ensure a single-turnover condition. Reactions were quenched at 2, 5, 10, 15, 30 and 75 min by adding 1.6 U proteinase K (New England Biolabs), 2 μl of 0.5 M EDTA and incubated for 45 min at 35 °C. Samples were denatured in formamide with trace bromophenol blue and xylene cyanol, run on a 15% denaturing polyacrylamide gel, visualized using Amersham Typhoon 5 Biomolecular Imager (GE Healthcare) and analyzed with ImageQuant (GE Healthcare) using peak area and rubberbanding for background deletion. All assays were carried out in triplicate to estimate experimental errors. The apparent cleavage rates (k_{obs}) from single-turnover assays were extracted from fitting the time-dependent products to the equation, $P(t) = P_F - P_F \times e^{-k_{obs} \times t}$, as described previously⁴², where P(t) and P_F are the fraction of mature miRNA at a given dicing

time point, t, and the reaction plateau, respectively. Due to slow processing of wild-type and GS constructs at low pH, their $P_{\rm F}$ values at high pH were used in data fitting, which is consistent with similar experimentally determined $P_{\rm F}$ values for ES substrate at both pH conditions. The population-weighted average (PWA) of maturation was calculated based on $P_{\rm PWA}(t) = p_{\rm GS} \times P_{\rm GS}(t) + p_{\rm ES} \times P_{\rm ES}(t)$, where $p_{\rm GS}$ are GS and ES populations, with $p_{\rm ES}$ being estimated at ~2% at pH7.77 and ~15% at pH 6.51 from NMR-derived parameters, and $P_{\rm GS/ES}(t)$ are the fractions of mature miRNAs from pre-miR-21^{GS} and pre-miR-21^{ES} at a given time point.

Preparation of RNA ladder for the sequencing gel. The ^{32}P -labeled pre-miR-21 substrate (2 µl), 3 µl of 0.1 µg µl $^{-1}$ yeast transfer RNA and 10 µl of 1× hydrolysis buffer (50 mM sodium carbonate pH 9.2, 1 mM EDTA) were combined in a single tube, and heated to 95 °C for 20 min. This tube was denatured in trace bromophenol blue and xylene cyanol before being loaded onto a 20% denaturing polyacrylamide gel.

RNA secondary structure prediction. All RNA secondary structures were predicted on the basis of sequences using the programs Mfold⁶⁰ and MC-Fold³⁹ using standard input options.

Reporting Summary. Further information on research design is available in the Nature Research Reporting Summary linked to this article.

Data availability

All data supporting the findings of this study are available in this published article, extended data and source data files.

Code availability

The in-house OriginLab scripts for data analyses are available upon request.

References

- Zhao, B., Hansen, A. L. & Zhang, Q. Characterizing slow chemical exchange in nucleic acids by carbon CEST and low spin-lock field R_{1ρ} NMR spectroscopy. J. Am. Chem. Soc. 136, 20–23 (2014).
- 47. Delaglio, F. et al. NMRpipe: a multidimensional spectral processing system based on UNIX pipes. *J. Biomol. NMR* 6, 277–293 (1995).
- Johnson, B. A. & Blevins, R. A. NMRView: a computer program for the visualization and analysis of NMR data. J. Biomol. NMR 4, 603–614 (1994).
- Zhao, B., Guffy, S. L., Williams, B. & Zhang, Q. An excited state underlies gene regulation of a transcriptional riboswitch. *Nat. Chem. Biol.* 13, 968–974 (2017).
- Kuhlman, B., Luisi, D. L., Young, P. & Raleigh, D. P. pK_a values and the pH dependent stability of the N-terminal domain of L9 as probes of electrostatic interactions in the denatured state. Differentiation between local and nonlocal interactions. *Biochemistry* 38, 4896–4903 (1999).
- Guenneugues, M., Berthault, P. & Desvaux, H. A method for determining B1 field inhomogeneity. Are the biases assumed in heteronuclear relaxation experiments usually underestimated? J. Magn. Reson. 136, 118–126 (1999).
- Vallurupalli, P., Bouvignies, G. & Kay, L. E. Studying "invisible" excited protein states in slow exchange with a major state conformation. *J. Am. Chem. Soc.* 134, 8148–8161 (2012).
- Mcconnell, H. M. Reaction rates by nuclear magnetic resonance. J. Chem. Phys. 28, 430–431 (1958).
- 54. Allard, P., Helgstrand, M. & Hard, T. The complete homogeneous master equation for a heteronuclear two-spin system in the basis of cartesian product operators. J. Magn. Reson. 134, 7–16 (1998).
- Helgstrand, M., Hard, T. & Allard, P. Simulations of NMR pulse sequences during equilibrium and non-equilibrium chemical exchange. *J. Biomol. NMR* 18, 49–63 (2000).
- Hansen, A. L. & Kay, L. E. Measurement of histidine pK_a values and tautomer populations in invisible protein states. *Proc. Natl Acad. Sci. USA* 111, E1705–E1712 (2014).
- Sekhar, A., Rosenzweig, R., Bouvignies, G. & Kay, L. E. Hsp70 biases the folding pathways of client proteins. *Proc. Natl Acad. Sci. USA* 113, E2794–E2801 (2016).
- Kolb, F. A. et al. Human dicer: purification, properties, and interaction with PAZ PIWI domain proteins. *Methods Enzymol.* 392, 316–336 (2005).
- DiNitto, J. P., Wang, L. & Wu, J. C. Continuous fluorescence-based method for assessing dicer cleavage efficiency reveals 3' overhang nucleotide preference. *BioTechniques* 48, 303–311 (2010).
- Zuker, M. Mfold web server for nucleic acid folding and hybridization prediction. *Nucleic Acids Res.* 31, 3406–3415 (2003).

Acknowledgements

We thank G. Young and S. Parnham for maintenance of NMR instruments and members of the Zhang laboratory for critical comments. This work was supported by a start-up fund and Jefferson Pilot Fellowship from the University of North Carolina at Chapel Hill and an NSF grant (MCB1652676).

Author contributions

J.T.B. and Q.Z. conceived the project and experimental design. J.T.B., J.A.B., B.Z., S.M.H. and Q.Z. prepared the samples. J.T.B., J.A.B., B.Z. and Q.Z. carried out NMR experiments, analyzed the data and wrote the paper.

Competing interests

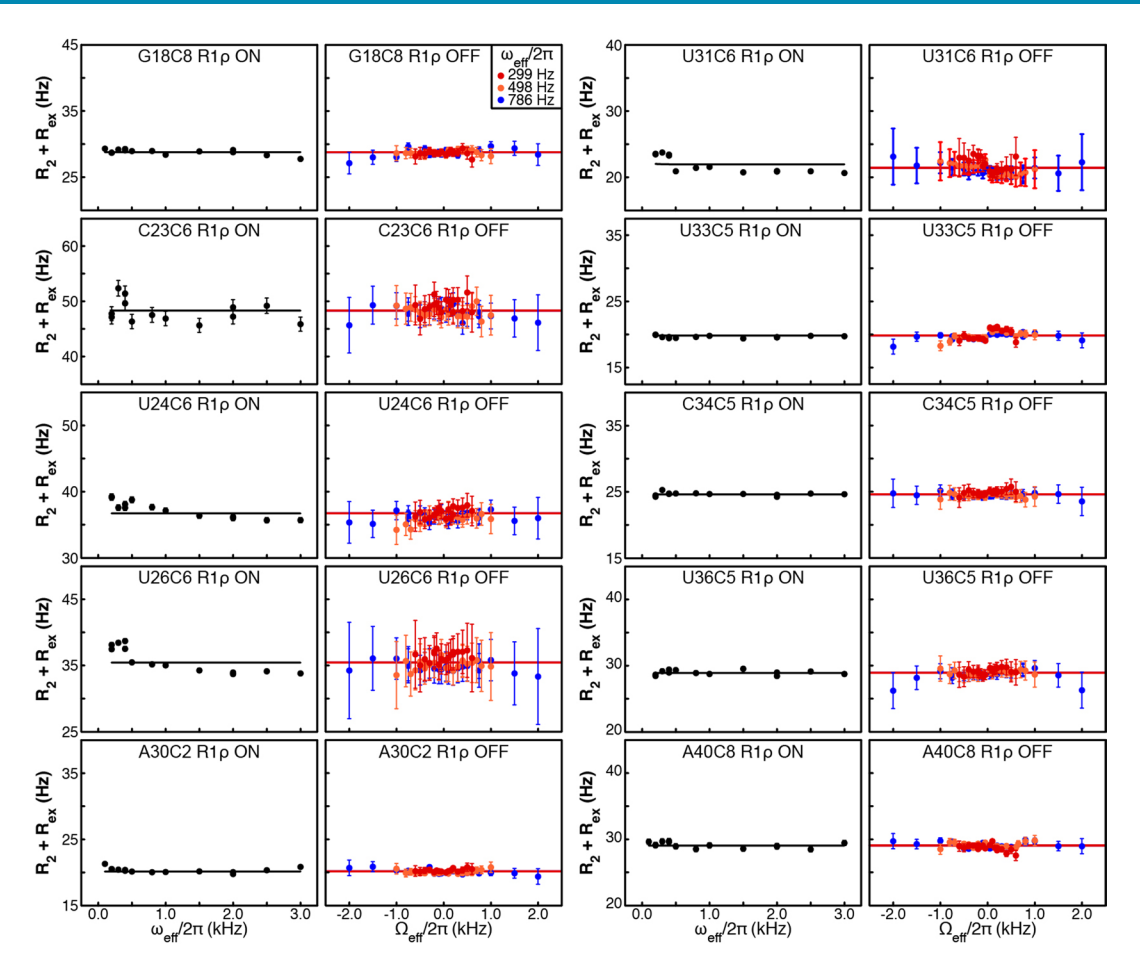
The authors declare no competing interests.

Additional information

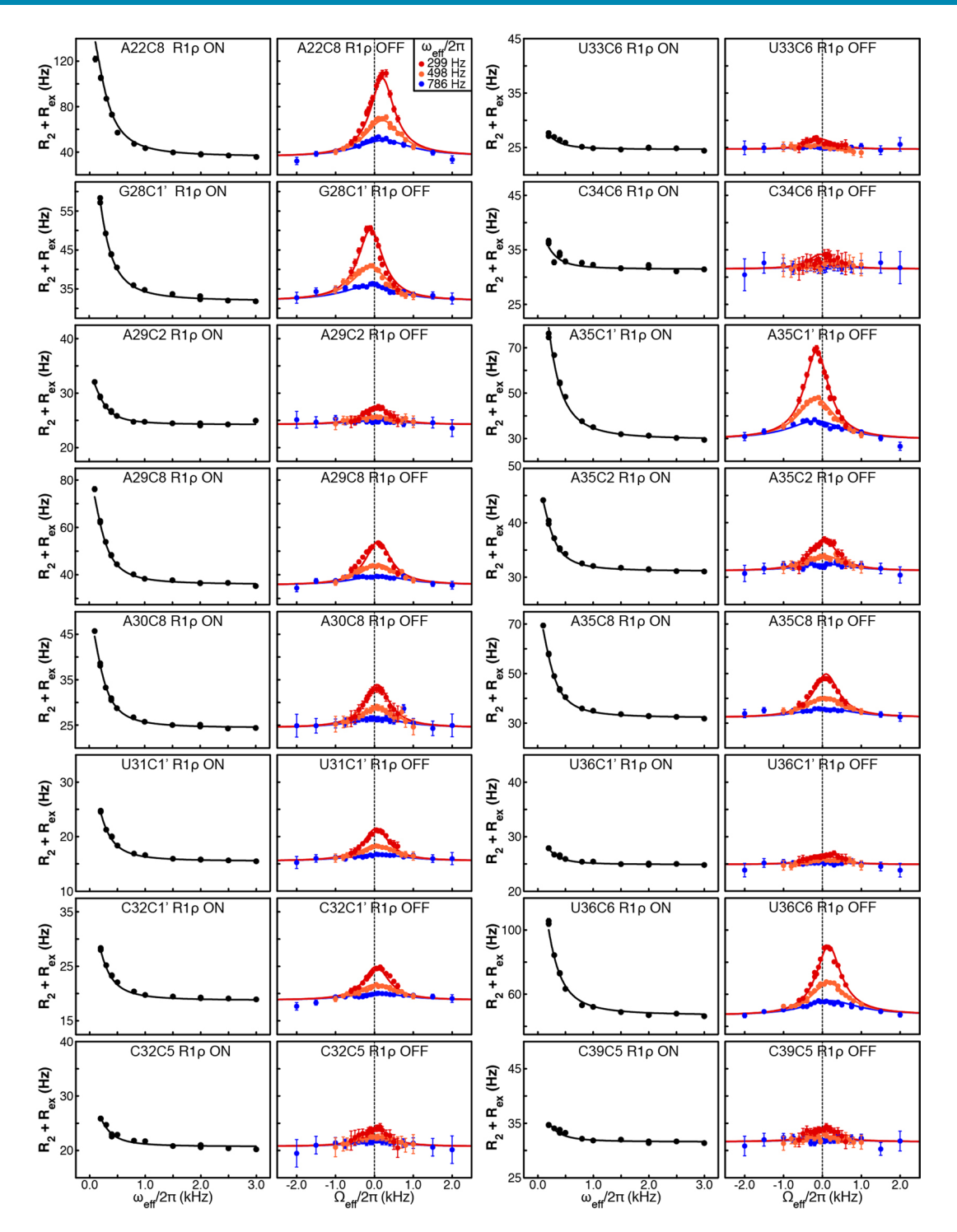
Extended data is available for this paper at https://doi.org/10.1038/s41589-020-00667-5. **Supplementary information** is available for this paper at https://doi.org/10.1038/s41589-020-00667-5.

Correspondence and requests for materials should be addressed to Q.Z.

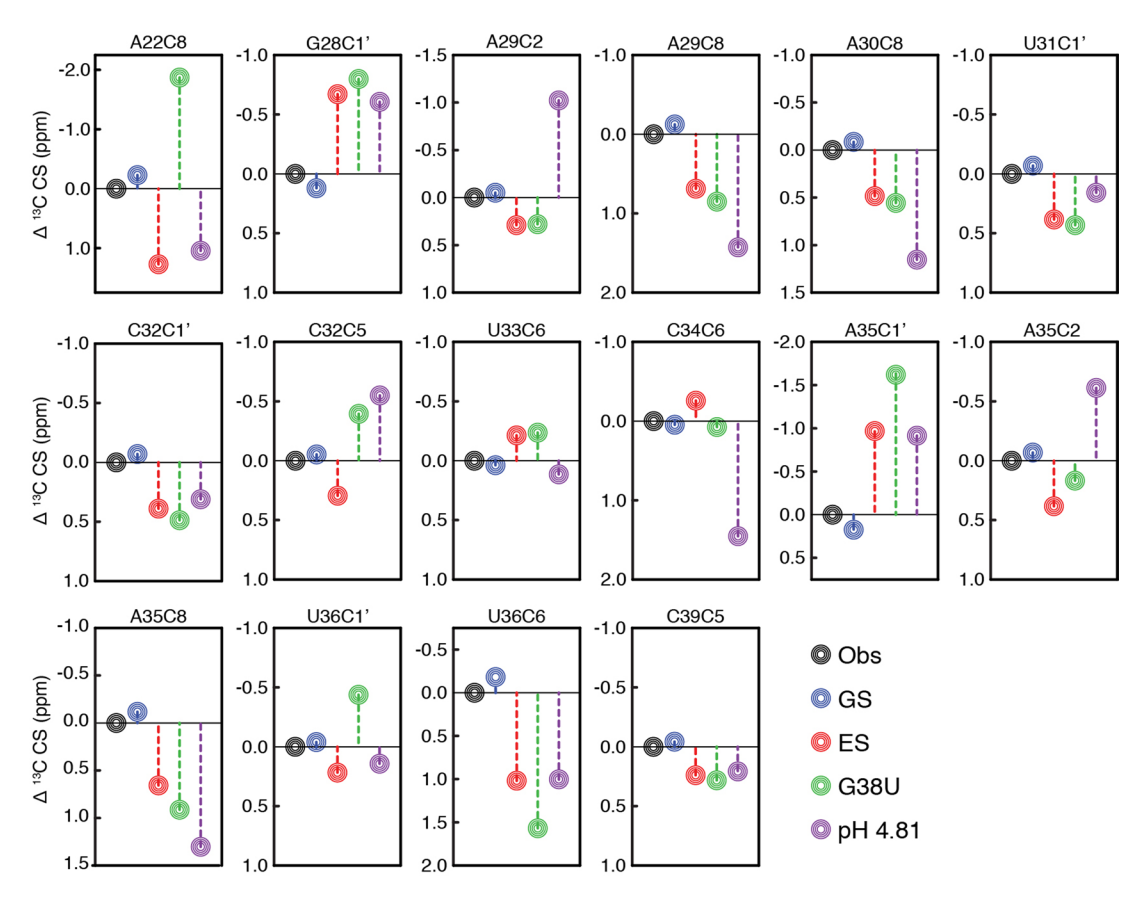
Reprints and permissions information is available at www.nature.com/reprints.



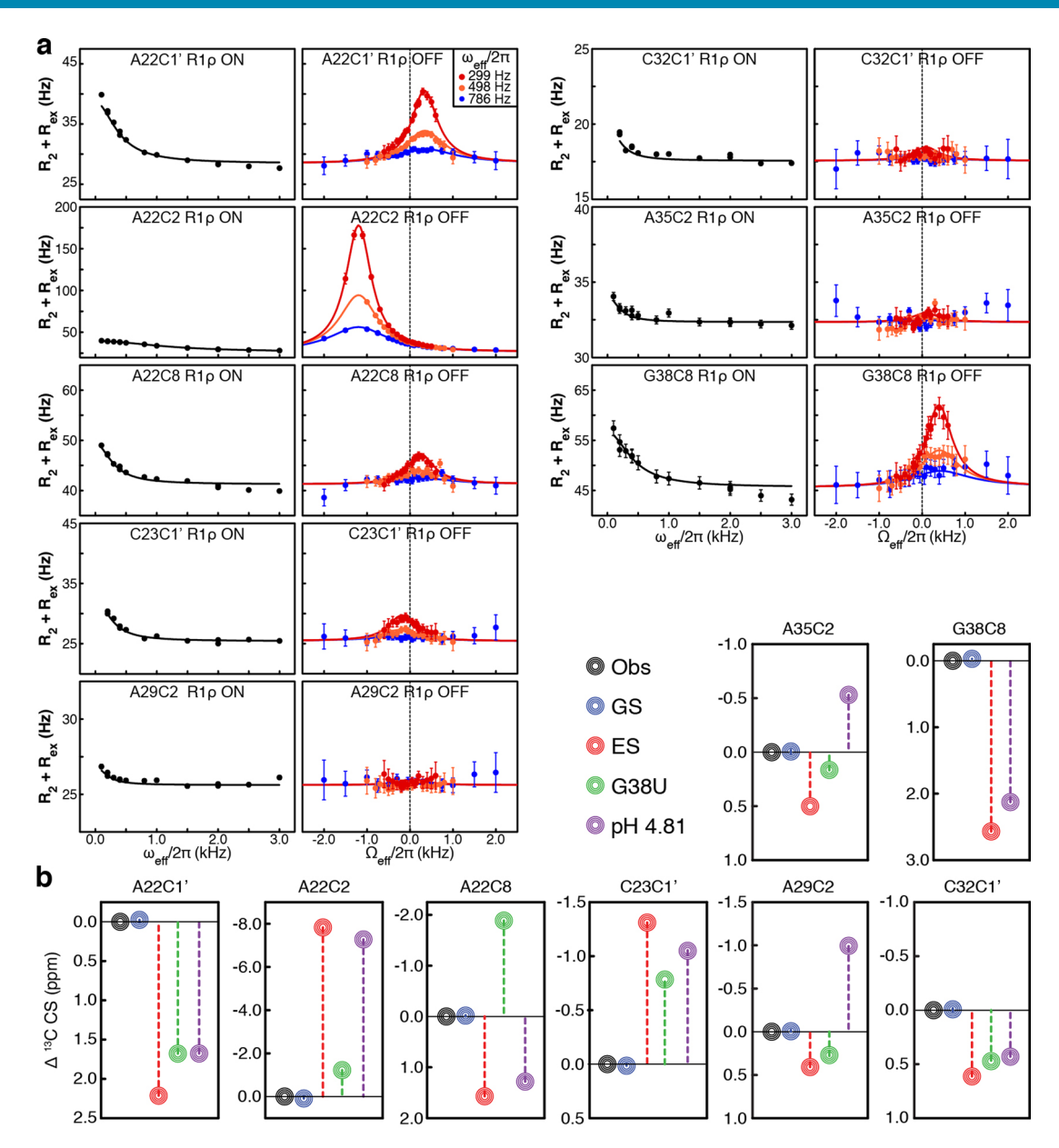
Extended Data Fig. 1 | ¹³C R_{1p} RD profiles of preE-miR-21 residues without apparent chemical exchange. On- and off-resonance ¹³C RD profiles depicting spin-lock power ($\omega_{eff}/2\pi$) and offset ($\Omega/2\pi$) dependence of $R_2 + R_{ex}$ measured at pH 6.45. Solid lines represent the best fits to a single-state model using the Bloch-McConnell equation. Shown are best-fit values and experimental uncertainties (s.d.) estimated from mono-exponential fitting of n=3 independently measured peak intensities.



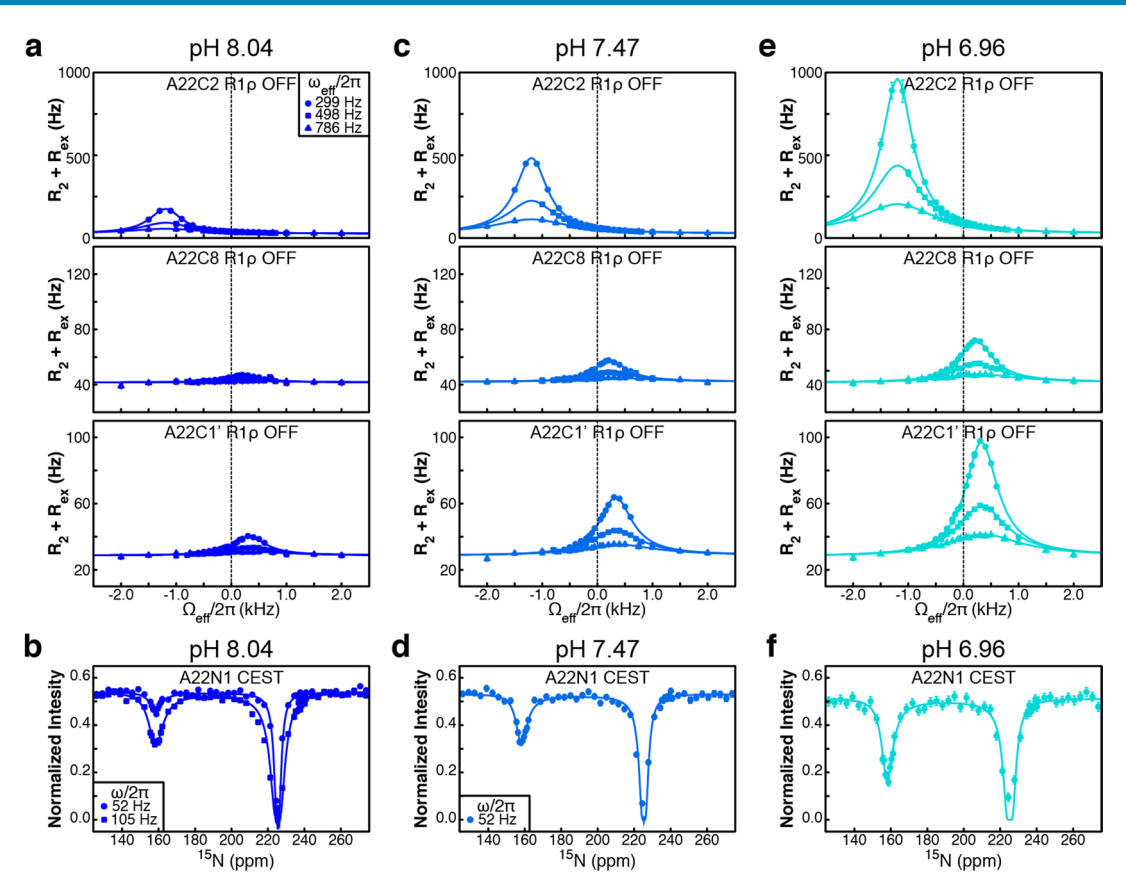
Extended Data Fig. 2 | ¹³C R_{1p} RD profiles of preE-miR-21 residues that undergo chemical exchange at pH 6.45. Solid lines represent the best fits to a global two-state exchange model ($k_{ex} = 1445 \pm 17 \, \text{s}^{-1}$ and $p_E = 15.2 \pm 0.3\%$) using the Bloch-McConnell equation. Shown are best-fit values and experimental uncertainties (s.d.) estimated from mono-exponential fitting of n = 3 independently measured peak intensities.



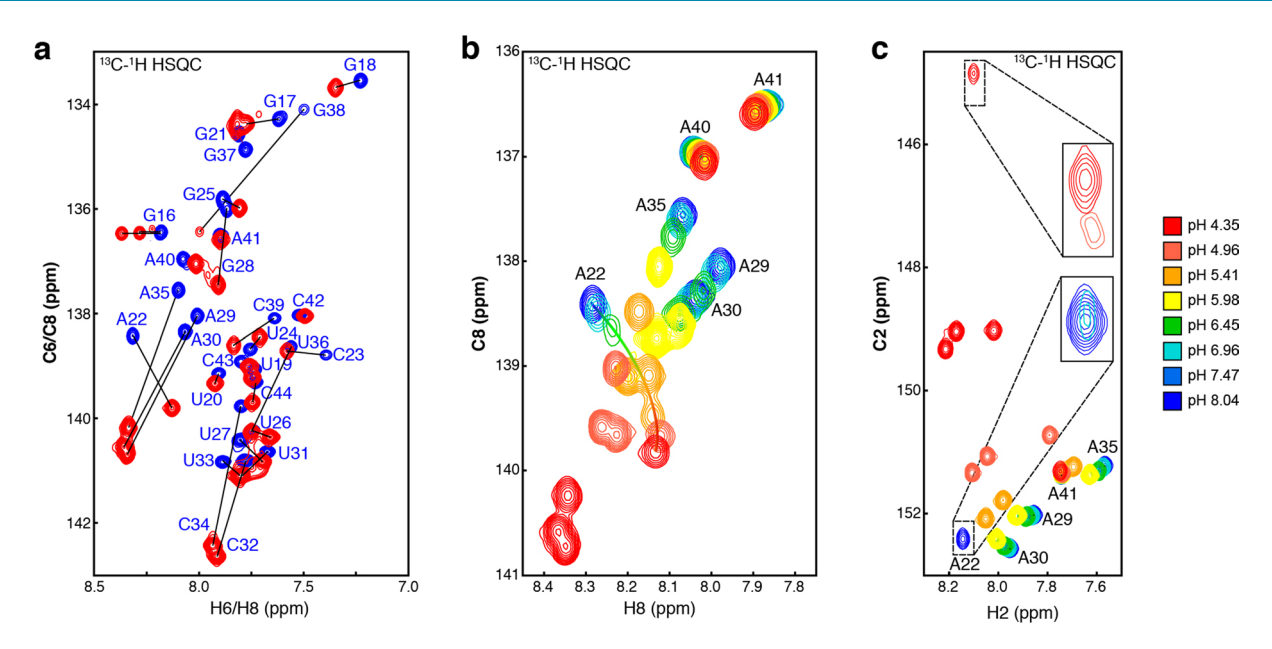
Extended Data Fig. 3 | Comparison of GS, ES, mutant carbon chemical shifts. Shown are differences between the observed chemical shifts (black) and the chemical shifts of GS (blue) and ES (red) extracted from 13 C R1p RD profiles at pH 6.45, G38U mutant at pH 6.45, and preE-miR-21 at pH 4.81. The apparent discrepancies between ES base carbon chemical shifts of A-C2/C8s and C-C5/C6s and their corresponding chemical shifts at pH 4.81 are likely due to intrinsic protonation at A-N1s and C-N3s at pH 4.81.



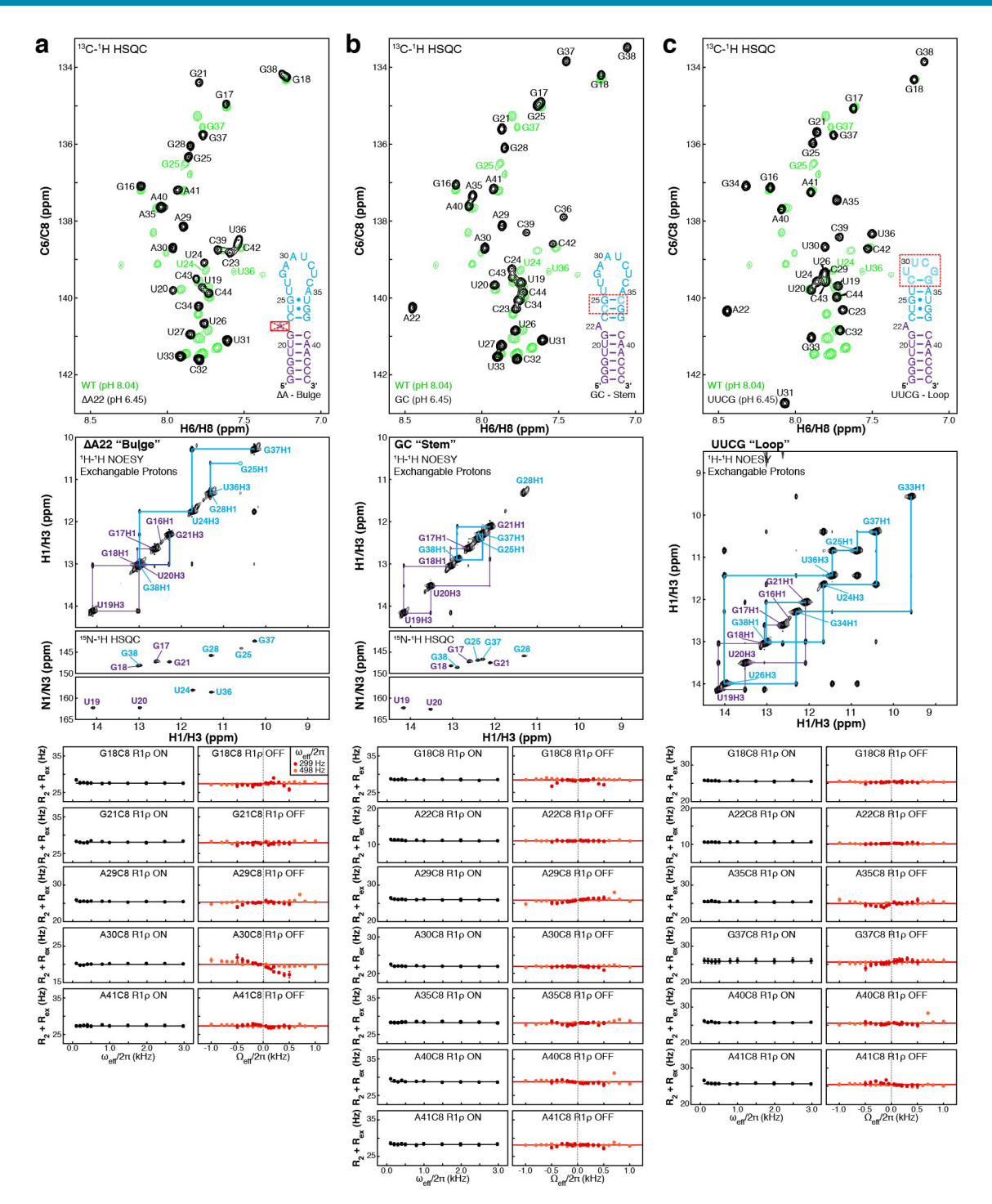
Extended Data Fig. 4 | ¹³C R_{1p} RD characterization of preE-miR-21 at pH 8.04. a, On- and off-resonance ¹³C RD profiles of residues that are exchange-broadened at lower pH points, including A22-C2, G38-C8, and G38-C1′. Solid lines represent the best fits to a global two-state exchange (k_{ex} = 1228 ± 51 s⁻¹ and p_{E} = $1.1 \pm 0.1\%$) using the Bloch-McConnell equation. **b**, Comparison of GS, ES, mutant carbon chemical shifts. Shown are differences between observed chemical shifts (black) and chemical shifts of GS (blue) and ES (red) extracted from ¹³C R_{1p} RD profiles at pH 8.04, G38U mutant at pH 6.45, and preE-miR-21 at pH 4.81. Shown are best-fit values and experimental uncertainties (s.d.) estimated from mono-exponential fitting of n = 3 independently measured peak intensities.



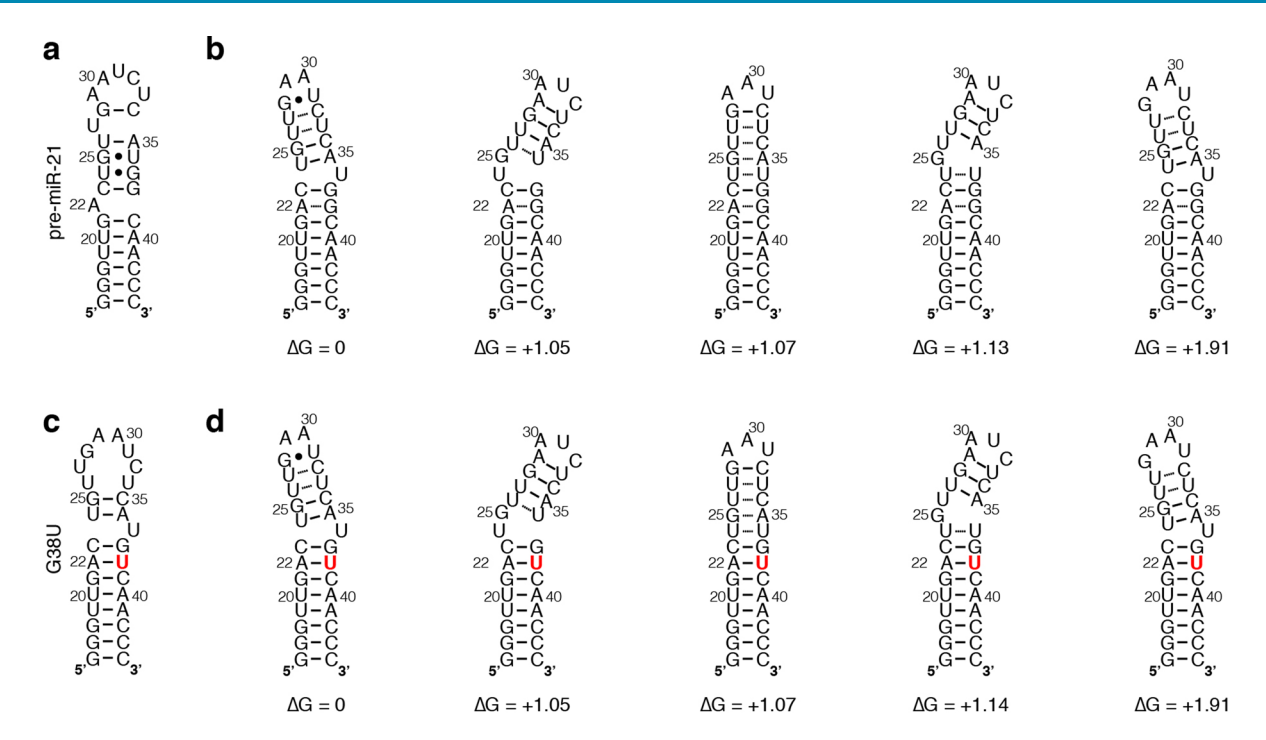
Extended Data Fig. 5 | NMR RD characterization of pH-dependent chemical exchange of residue A22. Shown are ¹³C R_{1p} RD profiles of A22-C2/C8/C1' and ¹⁵N CEST profile of A22-N1 at **a-b**, pH 8.04, **c-d**, pH 7.47, and **e-f**, pH 6.96. Solid lines represent the best fits to a global two-state exchange model at each individual pH condition using the Bloch-McConnell equation, resulting in $p_{\rm E} = 1.1 \pm 0.1\%$ at pH 8.04, $p_{\rm E} = 3.4 \pm 0.1\%$ at pH 7.47, and $p_{\rm E} = 6.4 \pm 0.1\%$ at pH 6.96. Shown are best-fit values and experimental uncertainties (s.d.) estimated from $p_{\rm E} = 1.1 \pm 0.1\%$ at pH 6.96. Shown are best-fit values and experimental uncertainties (s.d.) estimated from $p_{\rm E} = 1.1 \pm 0.1\%$ and pH 6.96. Shown are best-fit values and experimental uncertainties (s.d.) estimated from $p_{\rm E} = 1.1 \pm 0.1\%$ at pH 6.96. Shown are best-fit values and experimental uncertainties (s.d.) estimated from $p_{\rm E} = 1.1 \pm 0.1\%$ and pH 6.96. Shown are best-fit values and experimental uncertainties (s.d.) estimated from $p_{\rm E} = 1.1 \pm 0.1\%$ at pH 6.96. Shown are best-fit values and experimental uncertainties (s.d.) estimated from $p_{\rm E} = 1.1 \pm 0.1\%$ at pH 6.96. Shown are best-fit values and experimental uncertainties (s.d.) estimated from $p_{\rm E} = 1.1 \pm 0.1\%$ at pH 6.96. Shown are best-fit values and experimental uncertainties (s.d.) estimated from $p_{\rm E} = 1.1 \pm 0.1\%$ at pH 6.96. Shown are best-fit values and experimental uncertainties (s.d.) estimated from $p_{\rm E} = 1.1 \pm 0.1\%$ at pH 6.96. Shown are best-fit values and experimental uncertainties (s.d.) estimated from $p_{\rm E} = 1.1 \pm 0.1\%$ at pH 6.96. Shown are best-fit values and experimental uncertainties (s.d.) estimated from $p_{\rm E} = 1.1 \pm 0.1\%$ at pH 6.96. Shown are best-fit values and experimental uncertainties (s.d.) estimated from $p_{\rm E} = 1.1 \pm 0.1\%$ at pH 6.96. Shown are best-fit values and experimental uncertainties (s.d.) estimated from $p_{\rm E} = 1.1 \pm 0.1\%$ at pH 6.96. Shown are best-fit values at pH 6.96. Shown are best-fit



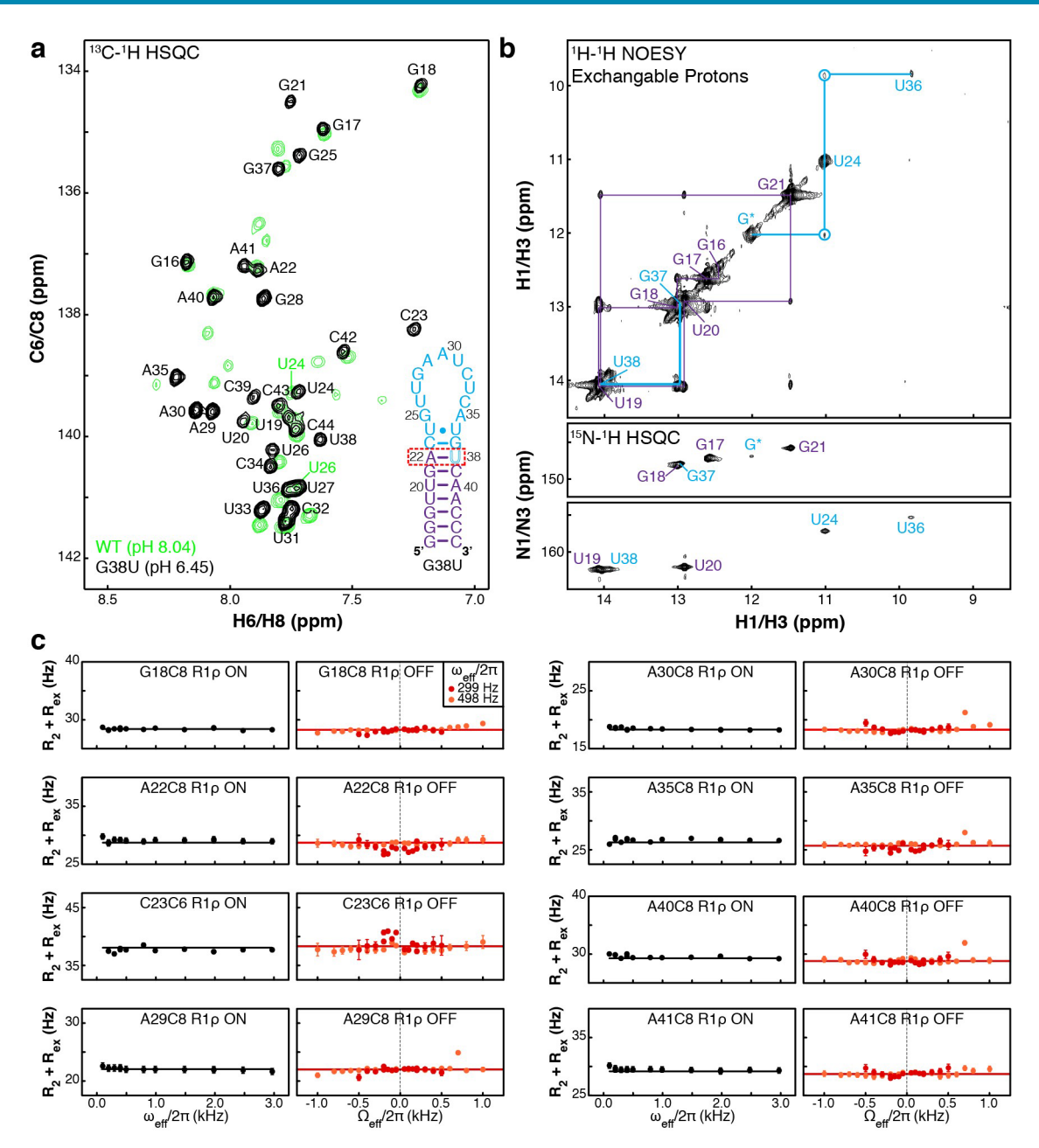
Extended Data Fig. 6 | NMR characterization of pH-dependent changes of preE-miR-21. a, ¹³C-¹H HSQC spectra of base carbons (C6 and C8) of uniformly ¹³C/¹⁵N-labeled preE-miR-21 at pHs 4.35 and 8.04 with mapping of chemical shift changes. **b**, ¹³C-¹H HSQC spectra of base carbons (C8) of adenine-specifically ¹³C/¹⁵N-labeled preE-miR-21 with pH ranging from 4.35 to 8.04. **c**, ¹³C-¹H HSQC spectra of base carbons (C2) of adenine-specifically ¹³C/¹⁵N-labeled preE-miR-21 with pH ranging from 4.35 to 8.04.



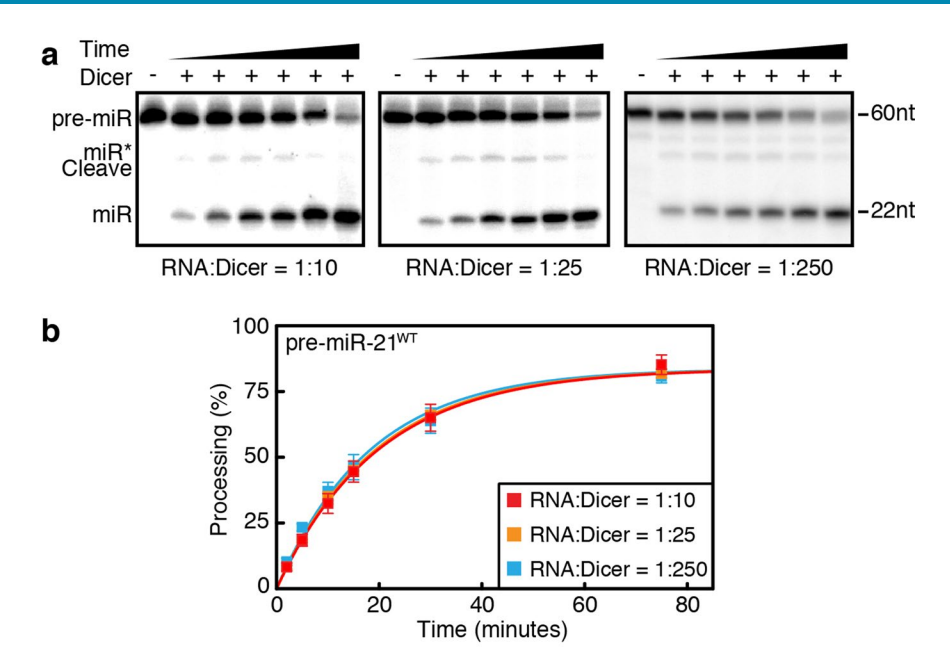
Extended Data Fig. 7 | NMR characterization of preE-miR-21 mutants. Shown are $^{13}C^{-1}H$ HSQC spectra of base carbons (C6 and C8) (black) that overlay with $^{13}C^{-1}H$ HSQC spectrum of WT preE-miR-21 at pH 8.04 (green) at 35°C, $^{1}H^{-1}H$ imino NOESY and $^{15}N^{-1}H$ HSQC spectra at 10°C, and ^{13}C R_{1p} RD profiles of uniformly $^{13}C/^{15}N$ -labeled **a**, $\Delta A22$ "bulge", **b**, GC "Stem", and **c**, UUCG "Loop" mutants at pH 6.45. Solid lines represent the best fits to a single-state model using the Bloch-McConnell equation. Shown are best-fit values and experimental uncertainties (s.d.) estimated from mono-exponential fitting of n = 3 independently measured peak intensities.



Extended Data Fig. 8 | Secondary structure prediction of preE-miR-21 and G38U mutant by Mfold and MC-Fold. a, M-fold predicted secondary structure of preE-miR-21, which contains G-U base pairs as observed in NMR data of the ground state. b, MC-Fold predicted secondary structures of preE-miR-21. Shown are the top 5 lowest-energy structures, ranked with ΔG relative to the lowest predicted structure. The A22-G38 base pair is predicted in all MC-Fold structures. c, M-fold predicted secondary structure of preE-miR-21 G38U mutant. d, MC-Fold predicted secondary structures of preE-miR-21 G38U mutant. Shown are the top 5 lowest-energy structures, ranked with ΔG relative to the lowest predicted structure. Both M-fold and MC-Fold predict the same lower stem structure of preE-miR-21 G38U mutant, which is also consistent with NMR data.



Extended Data Fig. 9 | NMR characterization of preE-miR-21 excited-state mimic. Shown are **a**, 13 C- 1 H HSQC spectrum of base carbons (C6 and C8) (black) that overlays with 13 C- 1 H HSQC spectrum of WT preE-miR-21 at pH 8.04 (green) at 35°C, **b**, 1 H- 1 H imino NOESY at 75 ms mixing time and 15 N- 1 H HSQC spectra at 10°C, and **c**, 13 C R_{1p} RD profiles of uniformly 13 C/ 15 N-labeled G38U mutant at pH 6.45. Solid lines represent the best fits to a single-state model using the Bloch-McConnell equation. Shown are best-fit values and experimental uncertainties (s.d.) estimated from mono-exponential fitting of n = 3 independently measured peak intensities.



Extended Data Fig. 10 | Single-turnover pre-miR-21 processing with 10-fold, 25-fold, and 250-fold excess Dicer enzyme. a, Single-turnover processing assays of recombinant human Dicer (500 nM) with pre-miR-21 at 50, 20, and 2 nM concentrations at pH 7.77 and 35 °C. **b**, Quantification of time-dependent Dicer processing of wild-type pre-miR-21 using ImageQuant. Solid lines represent best fits to a single exponential equation as described in Methods. Shown are mean values and standard deviations (s.d.) from n = 3 independent assays.



Corresponding author(s):	Qi Zhang
Last updated by author(s):	Aug 2, 2020

Reporting Summary

Nature Research wishes to improve the reproducibility of the work that we publish. This form provides structure for consistency and transparency in reporting. For further information on Nature Research policies, seeAuthors & Referees and theEditorial Policy Checklist.

_				
5	tэ	ŧι	ct	ICS

For	all st	tatistical analyses, confirm that the following items are present in the figure legend, table legend, main text, or Methods section.
n/a	Coi	nfirmed
	×	The exact sample size (n) for each experimental group/condition, given as a discrete number and unit of measurement
	×	A statement on whether measurements were taken from distinct samples or whether the same sample was measured repeatedly
	×	The statistical test(s) used AND whether they are one- or two-sided Only common tests should be described solely by name; describe more complex techniques in the Methods section.
×		A description of all covariates tested
×		A description of any assumptions or corrections, such as tests of normality and adjustment for multiple comparisons
	×	A full description of the statistical parameters including central tendency (e.g. means) or other basic estimates (e.g. regression coefficient AND variation (e.g. standard deviation) or associated estimates of uncertainty (e.g. confidence intervals)
	×	For null hypothesis testing, the test statistic (e.g. <i>F</i> , <i>t</i> , <i>r</i>) with confidence intervals, effect sizes, degrees of freedom and <i>P</i> value noted <i>Give P values as exact values whenever suitable.</i>
x		For Bayesian analysis, information on the choice of priors and Markov chain Monte Carlo settings
×		For hierarchical and complex designs, identification of the appropriate level for tests and full reporting of outcomes
x		Estimates of effect sizes (e.g. Cohen's d, Pearson's r), indicating how they were calculated
		Our web collection on statistics for biologists contains articles on many of the points above.

Software and code

Policy information about availability of computer code

Data collection

NMR data were collected on a Bruker Avance III 600 MHz spectrometer operated with software TOPSPIN 3.5 (Bruker). Gel images were collected on Amersham Typhoon 5 Biomolecular Imager (GE Healthcare).

Data analysis

NMR data were processed and analyzed with TOPSPIN 3.5 (Bruker) and publicly available software NMRPipe v7.1, NMRView v8.0.a15, and Sparky 3.110 (University of California, San Francisco, CA). In-house OriginLab scripts were used for NMR data fitting and are available upon request. Levenberg-Marquardt algorithm in OriginPro v9.1.0 (OriginLab) were used in NMR data fitting. Gel images were analyzed with Image Quant TL v8.2.0.0 (GE Healthcare). Online software Mfold (http://unafold.rna.albany.edu) and MC-Fold (https://major.iric.ca/MC-Fold/) were used to predict RNA secondary structures.

For manuscripts utilizing custom algorithms or software that are central to the research but not yet described in published literature, software must be made available to editors/reviewers. We strongly encourage code deposition in a community repository (e.g. GitHub). See the Nature Research guidelines for submitting code & software for further information.

Data

Policy information about availability of data

All manuscripts must include a data availability statement. This statement should provide the following information, where applicable:

- Accession codes, unique identifiers, or web links for publicly available datasets
- A list of figures that have associated raw data
- A description of any restrictions on data availability

The authors declare that the data supporting the findings of this study are available within the article, extended data and source data files, or are available upon reasonable request.

Field-specific reporting					
Please select the or	ne below that is the best fit for your research. If you are not sure, read the appropriate sections before making your selection.				
🗶 Life sciences	Behavioural & social sciences				
For a reference copy of t	he document with all sections, see <u>nature.com/documents/nr-reporting-summary-flat.pdf</u>				
Life sciences study design					
All studies must dis	close on these points even when the disclosure is negative.				
Sample size	For in vitro Dicer processing assays, sample size of N=3 was used to obtained statistics, which was chosen based on community standards. Predetermination of sample size was not necessary for these in vitro quantitative biochemical experiments.				
Data exclusions	No data exclusions.				
Replication	N =3 replicates were performed for in vitro Dicer processing assays. All attempts at replication were successful. RNA samples and enzyme were prepared multiple times, and produced similar results in the in vitro biochemical assays.				
Randomization	No randomization was used in this study, as the experiments were quantitative in vitro biochemical assays.				
Blinding	linding No blinding was used in this study, as objective, quantitative biochemical experiments were performed and samples were treated identically				
Reportin	g for specific materials, systems and methods				
We require information	on from authors about some types of materials, experimental systems and methods used in many studies. Here, indicate whether each material, sed is relevant to your study. If you are not sure if a list item applies to your research, read the appropriate section before selecting a response.				
Materials & exp	perimental systems Methods				
n/a Involved in th	e study n/a Involved in the study				
Antibodies					
Eukaryotic					
	Palaeontology MRI-based neuroimaging				
Animals and other organisms X Human research participants					